Physics and Detector Performance Metrics for the GlueX Experiment

GlueX-doc-1063-v2

1 Introduction

We start this report on the GlueX detector by discussing the physics goals of the GlueX project, which focuses on mapping the spectrum of gluonic excitations, starting with exotic hybrid mesons produced using a beam of 9 GeV linearly polarized photons. We show that the search for exotic mesons depends critically on detecting and measuring the four-momenta of charged particles and photons resulting from the decays of photoproduced mesons. As will be discussed in this report, the majority of the final states to be studied in GlueX involve a combination of both charged particles and photons. Thus, the design of the GlueX detector has taken a unified approach to assure good acceptance and resolution for detection of all particles. We then review the existing photoproduction data, where the extremely low statistics and limited capabilities (for neutrals) of older experiments indicate that very little is known about the physics to be studied in GlueX [1, 2].

The detector requirements on GlueX are driven by the need to identify exclusive reactions in order to perform the amplitude analysis that will extract meson quantum numbers, J^{PC}, and the need to be sensitive to a variety of meson decay modes. Generally speaking, an amplitude analysis needs a large and uniform acceptance detector with resolution sufficient for cleanly separating final states. This reduces background leakage into the reactions of interest. In order to demonstrate that the GlueX experiment will be capable of carrying out its physics goals, we compare the capabilities of GlueX with the successful Brookhaven E852 experiment. We show that for the kinematic quantities of interest in the GlueX analyses, the performance is GlueX is very comparable to E852Ẇith similar statistics as E852, the search in for exotic mesons can be carried out in GlueX at least as well as E852Ṫhis coupled with the both the sparseness of existing photoproduction data, and the much higher statistics expected in GlueX, leads us to conclude that GlueX has an excellent chance of discovering and mapping exotic mesons if they exist.

In the latter part of this report are shown the underlying detector performances that lead to the above conclusions. For much of the physics of exotic mesons, being able to separate pions from protons is necessary. Information of the individual particle identification systems as well as information on more sophisticated global analyses is discussed. The separation of pions and protons will be very good in GlueX, while the clean identification of kaons will be difficult using the existing particle identification detectors alone. This report also summarizes information on the performance of the tracking chambers that are used to reconstruct charged particles in GlueX. This includes the information on how the position resolution of the chambers translates into momentum resolution and a summary of the expected kinematics in GlueX and how it maps onto the tracking elements of the detector.

The GlueX detector uses a geometry based on solenoidal magnetic field, this is ideal for a fixed-target photoproduction experiment (Figure 1). The solenoidal magnetic field traps low energy electromagnetic backgrounds (e^+e^- pairs) generated in the target inside a cone around the beam. It also allows for effective instrumentation of calorimeters to achieve very high acceptance for photons. The superconducting solenoid produces a 2.25 T field. A tagged, ≈ 9 GeV, linearly polarized photon beam is incident on a 30 cm long liquid-hydrogen target that is surrounded by a start counter which is used in triggering. Next is a cylindrical tracking chamber, the CDC, and then a cylindrical electromagnetic calorimeter, the BCAL. Downstream of the CDC are four packages of circular planar drift chambers, FDC, followed by a time-of-flight wall, TOF. This is followed by a circular planar electromagnetic calorimeter, the FCAL. Space has been reserved between the downstream end of the magnet and the TOF for a possible particle identification (PID) system. This design provides for nearly 4π acceptance for both charged particles and photons. While the

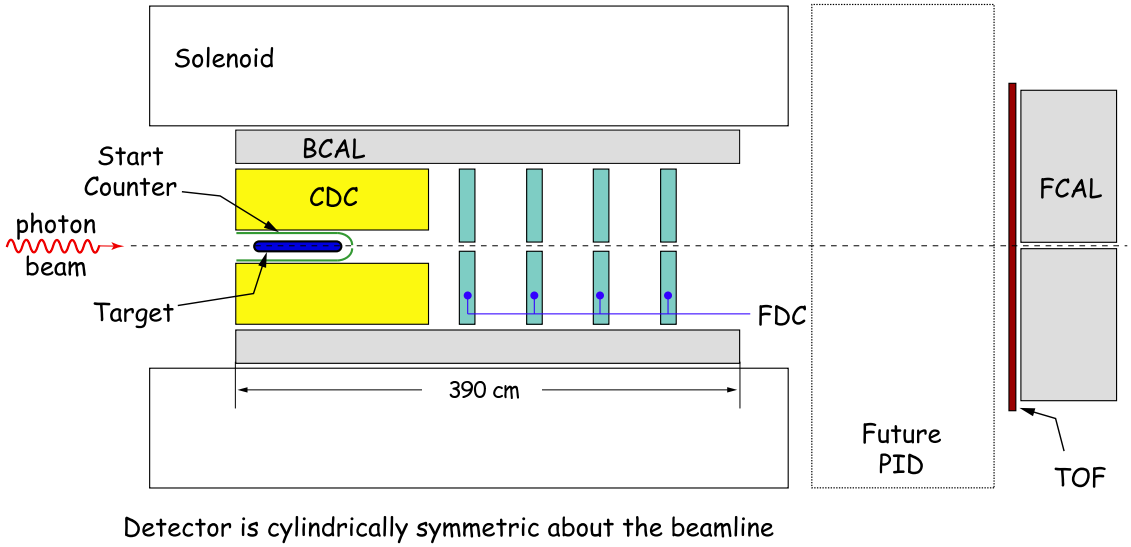

Figure 1: Schematic of the GlueX detector. A description is provided in the text.

acceptance is not completely uniform in all variables, there are no holes in the kinematic variables of interest.

2 Physics Motivation: the search for exotic mesons

2.1 QCD and light meson spectroscopy

The observation, nearly four decades ago, that mesons are grouped in nonets, each characterized by unique values of J^{PC} – spin (J), parity (P) and charge conjugation (C) quantum numbers – led to the development of the quark model. Within this picture, mesons are bound states of a quark (q) and antiquark ($\bar{q}$). The three light-quark flavors (*up*, *down* and *strange*) suffice to explain the spectroscopy of most – but not all – of the lighter-mass mesons (below 3 GeV/c^2) that do not explicitly carry heavy flavors (charm or beauty). Early observations yielded only those J^{PC} quantum numbers consistent with a fermion-antifermion bound state. The J^{PC} quantum numbers of a $q\bar{q}$ system with total quark spin, $\vec{S}$, and relative angular momentum, $\vec{L}$, are determined as follows: $\vec{J} = \vec{L} + \vec{S}$, $P = (-1)^{L+1}$ and $C = (-1)^{L+S}$. Thus J^{PC} quantum numbers such as 0^{--}, 0^{+-}, 1^{-+} and 2^{+-} are not allowed and are called *exotic* in this context.

Our understanding of how quarks form mesons has evolved within quantum chromodynamics (QCD) and we now expect a richer spectrum of mesons that takes into account not only the quark degrees of freedom, but also the gluonic degrees of freedom. Gluonic mesons with no quarks (*glueballs*) are expected. These are bound states of pure glue, and since the quantum numbers of low-lying glueballs (below 4 GeV/c^2) are not exotic, they should manifest themselves as extraneous states that cannot be accommodated within $q\bar{q}$ nonets. But their unambiguous identification is complicated by the fact that they can mix with $q\bar{q}$. Excitations of the gluonic field binding the quarks can also give rise to so-called *hybrid* mesons that can be viewed as bound states of a quark, antiquark and valence gluon ($q\bar{q}g$). An alternative picture of hybrid mesons, one supported by lattice QCD [3], is one in which a gluonic flux tube forms between the quark and antiquark and the excitations of this flux tube lead to so-called *hybrid* mesons. Actually the idea of flux tubes, or strings connecting the quarks, originated in the early 1970's [4] to explain the observed linear dependence of the mass-squared of hadrons on spin (Regge trajectories). Conventional $q\bar{q}$ mesons arise when the flux tube is in its ground state, while hybrid mesons arise when the flux tube is excited. Particularly interesting is that some of these hybrid mesons can have a unique signature, exotic J^{PC}. The spectroscopy of these exotic hybrid mesons is simplified because they do not mix with conventional $q\bar{q}$ states.

The level splitting between the ground state flux tube and the first excited transverse modes is π/r, where r is the separation between the quarks, so the hybrid spectrum should lie about 1 GeV/c^2 above the ground state spectrum. While the flux-tube model [5] has all hybrid nonets degenerate in mass, from lattice gauge calculations [6], one expects the lightest exotic hybrid (the $J^{PC} = 1^{-+}$) to have a mass of about 1.9 GeV/c^2. In this discussion, the motion of the quarks was ignored, but we know from general principles [5] that an approximation that ignores the impact of the flux tube excitation and quark motion on each other seems to work quite well. It should be noted, also, in the large-N_c limit of QCD, exotic hybrids are expected to have narrow widths, comparable to $q\bar{q}$ states [7]. To be able to map out the spectrum of exotic hybrids, it is important to be able to observe mesons with a mass of ≈ 2.5 GeV/c^2, which requires a mass reach up to about 2.8 GeV/c^2.

In the coming years there will be significant computational resources dedicated to understanding non-perturbative QCD, including confinement, using lattice techniques. The prediction of the hybrid spectrum, including decays, will be a key part of this program, but experimental data will be needed to verify these calculations. The spectroscopy of exotic mesons provides a clean and

attractive starting point for the study of gluonic excitations.

The GlueX experiment is designed to collect high quality and high statistics data on the photoproduction of light mesons. As part of the program of identifying exotic hybrid mesons, these data will also be used to understand the conventional meson spectrum, including the poorly understood excited vector mesons.

2.2 Using linearly polarized photons

There are tantalizing suggestions, mainly from experiments using beams of π mesons, that exotic hybrid mesons exist. The evidence is by no means clear cut, owing in part, to the apparently small production rates for these states in the decay channels examined. It is safe to conclude that the extensive data collected to date with π probes have not uncovered the hybrid meson spectrum. (A recent paper by E. Klempt and A. Zaitsev gives an encyclopedic and critical overview of the current experimental situation with regard to searches for glueballs, hybrids and multiquark mesons [8].) Models, like the flux-tube model, however, indicate the photon is a probe that should be particularly effective in producing exotic hybrids.

The first excited transverse modes of the flux tube are degenerate and correspond to clockwise or counterclockwise rotations of the flux tube around the axis joining the quark and antiquark fixed in space with $J = 1$ [5]. Linear combinations of these two modes are parity eigenstates and lead to $J^{PC} = 1^{+-}$ and $J^{PC} = 1^{-+}$ for the excited flux tube. When these quantum numbers are combined with those of the $q\bar{q}$ with $\vec{L} = 0$ and $\vec{S} = 1$ (quark spins aligned), three of the six possible J^{PC} have exotic combinations: 0^{+-}, 1^{-+} and 2^{+-}. A photon probe is a virtual $q\bar{q}$ with quark spins aligned. In contrast, when the $q\bar{q}$ have $\vec{L} = 0$ and $\vec{S} = 0$ (spins anti-aligned), the resulting quantum numbers of the hybrid meson are not exotic. Pion probes are $q\bar{q}$ with quark spins anti-aligned. If we view one outcome of the scattering process as exciting the flux tube binding the quarks in the probe, the suppression of exotic hybrids in π-induced reactions is not surprising – a spin flip of one of the quarks is required followed by the excitation of the flux tube. In contrast, the spins of the virtual quarks in the photon probe are properly aligned to lead to exotic hybrids. Phenomenological studies quantitatively support this picture predicting that the photoproduction cross sections for exotic mesons are comparable to those for conventional mesons [9].

Determining the quantum numbers of mesons produced in the GlueX experiment will require an amplitude analysis based on measuring the energy and momentum of their decay products. Linear polarization of the incident photon is required for a precision amplitude analysis to identify exotic quantum numbers, to understand details of the production mechanism of exotic and conventional mesons and to remove backgrounds due to conventional processes. Linear polarization will be achieved using the coherent bremsstrahlung technique.

For the GlueX solenoid-based detector system, given the mass reach required (up to 2.8 GeV/c^2) for mapping the spectrum of exotic hybrid mesons, a photon energy of ≈ 9 GeV is ideal. The requisite degree of linear polarization for 9 GeV photons can be achieved using coherent bremsstrahlung, but requires a minimum electron energy of 12 GeV.

2.3 Expected decay modes of exotic hybrid mesons

Table 1 lists predicted J^{PC} exotic mesons and their decay modes. According to the flux tube model and verified by lattice QCD [10], the preferred decay modes for exotic hybrids are into $(q\bar{q})_P + (q\bar{q})_S$ mesons such as $b_1\,\pi$ or $f_1\,\pi$ (the subscripts P and S refer to the orbital angular momentum between

the quark and antiquark in the meson). Table 2 lists candidate exotic $J^{PC} = 1^{-+}$ states for which evidence has been claimed. The purported exotic states include decay modes into $b_1\,\pi$ or $f_1\,\pi$, as well as decay modes into $\eta\,\pi$ and $\eta'\,\pi$. The dominant branching fractions for meson states listed among the decay products are summarized in Table 3. Clearly, exotic meson spectroscopy requires the ability to detect and measure charged particles, as well as π^0 and η mesons.

Most of the preferred or observed exotic hybrid decay modes listed in Tables 1 and 2 involve several pions. These will occur in final states that only involve $\pi^{\pm}$ such as $(\rho\pi)^+ \to \pi^+\pi^+\pi^-$, but also in combinations which include π^0s, $(\rho\pi)^+ \to \pi^+\pi^0\pi^0$. Having all the isospin related final states available provides an extremely important isospin consistency checks of the amplitude analysis and understanding of the detector acceptance.

Exotic Meson	J^{PC}	I	G	Possible Modes
b_0	0^{+-}	1	+	
h_0	0^{+-}	0	−	$b_1\pi$
π_1	1^{-+}	1	−	$\rho\pi$, $b_1\pi$
η_1	1^{-+}	0	+	$a_2\pi$
b_2	2^{+-}	1	+	$a_2\pi$
h_2	2^{+-}	0	−	$\rho\pi$, $b_1\pi$

Table 1: Predicted J^{PC} exotic hybrid mesons and their expected decay modes. See Table 3 for decay modes of the b_1 and a_2 mesons.

Exotic Meson Candidate	Decay Mode
$\pi_1(1400)$	$\pi^-\eta$
	$\pi^0\eta$
$\pi_1(1600)$	$\rho^0\pi^-$
	$\eta'\pi^-$
$\pi_1(1600/2000)$	$b_1\pi$
	$f_1\pi$

Table 2: Reported $J^{PC} = 1^{-+}$ exotic hybrid mesons and their decay modes. See Table 3 for decay modes of the η', b_1 and f_1 mesons. Source: 2006 Review of Particle Physics [11].

2.4 Information from existing photoproduction data

There is little data on meson photoproduction in the GlueX energy regime ($E_\gamma \approx 7 - 9$ GeV). Almost all of what is known comes from bubble chamber measurements at SLAC [12, 13, 14, 15, 16, 17]. These experiments were among the first exploratory studies of the photoproduction of meson and baryon resonances at these energies, and although they suffer from low-statistics, they have good acceptance, except for events with multiple neutrals. Exclusive reactions leading to final states with charged particles and a single neutron or π^0 can be identified by kinematic fitting. Table 4 summarizes the photoproduction cross sections for various charged particle topologies, with and without neutrals, at $E_\gamma = 9.3$ GeV [12]. Final states with single or multi-neutral particles (π^0, η or n) account for about 82% of the total cross section. About 13% of the total cross section is due to

Meson Decay Mode	Branching Fraction (%)
$\pi^0 \to 2\gamma$	99
$\eta \to 2\gamma$	39
$\eta \to 3\pi^0$	33
$\eta \to \pi^+\pi^-\pi^0$	23
$\omega \to \pi^+\pi^-\pi^0$	89
$\omega \to \pi^0\gamma$	9
$\eta' \to \pi^+\pi^-\eta$	45
$\eta' \to \pi^0\pi^0\eta$	21
$\eta' \to 2\gamma$	2
$b_1(1235) \to \omega\pi$	dominant
$f_1(1285) \to \pi^0\pi^0\pi^+\pi^-$	22
$f_1(1285) \to \eta\pi\pi$	52
$a_2(1320) \to 3\pi$	70
$a_2(1320) \to \eta\pi$	15

Table 3: Neutral or charged + neutral decay modes of several well established mesons. Source: 2006 Review of Particle Physics [11].

final states with charged particles and a single π^0. So for about 70% of the total photoproduction cross section, from $E_\gamma \approx 7$ to ≈ 12 GeV, we have essentially no information. Extrapolating from what is known from the final states that have been identified and studied, the bulk of the unknown processes are expected to involve final states with combinations of π^0 and η mesons. The discovery potential of GlueX rests on being able to detect π^0 and η mesons in addition to charged particles.

Topology	σ (μb)	% of σ with neutrals
1-prong	8.5 ± 1.1	100
3-prong	64.1 ± 1.5	76 ± 3
5-prong	34.2 ± 0.9	86 ± 4
7-prong	6.8 ± 0.3	86 ± 6
9-prong	0.61 ± 0.08	87 ± 21
With visible strange decay	9.8 ± 0.4	-
Total	124.0 ± 2.5	82 ± 4

Table 4: Topological photoproduction cross sections for γp interactions at 9.3 GeV from Reference [12]. Also shown are the percent of the cross section with neutral particles for each topology.

2.5 Studies using PYTHIA

As noted above, much is unknown about photoproduction at GlueX energies leading to multi-neutral final states. To estimate photon yields, we used the Monte Carlo program PYTHIA [18] that was written to generate high-energy physics events produced in a wide variety of initial states, including fixed target photoproduction. The program is based on a combination of analytical results and QCD-based models of particle interactions. PYTHIA was designed to allow for tuning

parameters to suit the particular situation – for example, photoproduction at 9 GeV. The output of the simulations was compared [19] to published data, in particular, reference [12]. Comparison of cross section estimates for charged particle topologies and several reactions in the 3-prong and 5-prong final states, which account for 80% of the total cross section, are shown in Tables 5 and 6. The vector mesons ρ, ω and ϕ appear in the 3-prong sample in the $\pi^+\pi^-p$, $\pi^+\pi^-\pi^0p$ and K^+K^-p final states, respectively. The distribution in $|t|$ for PYTHIA events agrees with published data for specific reactions. PYTHIA also accounts for Δ resonance production. In the $\pi^+\pi^-K^+K^-p$ state, the $K^*(890)$ is present in PYTHIA.

Topology	PYTHIA Estimates (μb)	Data (μb)
1-prong	8.8 ± 0.02	8.5 ± 1.1
3-prong	63.5 ± 0.09	64.1 ± 1.5
5-prong	42.7 ± 0.2	34.2 ± 0.9
7-prong	7.3 ± 0.1	6.8 ± 0.3
9-prong	0.3 ± 0.1	0.61 ± 0.08

Table 5: Topological photoproduction cross sections at 9 GeV from PYTHIA and from bubble chamber data [12]. The PYTHIA cross section estimates have been normalized to a total photoproduction cross section of 124 μb. The errors on the PYTHIA estimates are statistical.

Reaction	PYTHIA Estimates (μb)	Data (μb)
	$\gamma p \to 3$ prongs	
$\gamma p \to p\pi^+\pi^-$	13.6 ± 0.13	14.7 ± 0.6
$\gamma p \to pK^+K^-$	0.41 ± 0.02	0.58 ± 0.05
$\gamma p \to p\bar{p}p$	0.04 ± 0.01	0.09 ± 0.02
$\gamma p \to p\pi^+\pi^-\pi^0$	5.8 ± 0.1	7.5 ± 0.8
$\gamma p \to n2\pi^+\pi^-$	1.4 ± 0.04	3.2 ± 0.7
With multi-neutrals	42.3 ± 0.3	38.0 ± 1.9
	$\gamma p \to 5$ prongs	
$\gamma p \to p2\pi^+2\pi^-$	2.9 ± 0.06	4.1 ± 0.2
$\gamma p \to pK^+K^-\pi^+\pi^-$	0.51 ± 0.03	0.46 ± 0.08
$\gamma p \to p2\pi^+2\pi^-\pi^0$	8.12 ± 0.1	6.7 ± 1.0
$\gamma p \to n3\pi^+2\pi^-$	$0.8 \pm .3$	1.8 ± 1.9
With multi-neutrals	30.4 ± 0.2	21.1 ± 1.7

Table 6: Photoproduction reaction cross sections at 9 GeV from PYTHIA and from bubble chamber data [12]. The PYTHIA cross section estimates have been normalized to a total photoproduction cross section of 124 μb. The errors on the PYTHIA estimates are statistical.

Photoproduction of meson resonances in the GlueX energy regime typically result in the meson being produced at small absolute values of the momentum transfer squared $|t|$ between the incoming photon and the outgoing meson – or equivalently between the target proton and the recoil nucleon or baryon resonance. The produced meson, as well as its decay products (depending on the particle multiplicity and relative mother-daughter masses), move in the forward direction, whereas the recoil baryon moves at large angles $\gtrsim 45^\circ$ with respect to the beam direction. If the recoil baryon

is a resonance, such as a Δ or N^*, decays involving pions will occur. These baryon-resonance reactions are also expected to be a fruitful place to search for exotic hybrids. GlueX will be able to exclusively identify these final states, by detecting the soft, wide-angle pion from the resonance decay.

Photoproduction of mesons using a ≈ 9 GeV, linearly polarized photon beam provides a unique opportunity to search for exotic hybrids. Existing data is extremely limited for charged final states, and no data exist for multi-neutral final states. To carry out such a search, GlueX will need to look at many different final states involving both charged particles and photons, but particular emphasis will be placed on those reactions that have 3 or more pions in the final state. The discovery potential for GlueX comes first from the very high statistics (at least 10^7 tagged photons per second on target), which will exceed existing photoproduction data by 4 to 5 orders of magnitude, (and even the best spectroscopy experiments to date by 1 to 2 orders of magnitude). Second, GlueX has the ability to study many different final states in the same detector. These two effects will not only identify hybrids if they exist, but also map out their decay properties.

3 Physics analysis in GlueX

The ultimate goal of the GlueX experiment is to identify exotic mesons by an amplitude analysis of exclusive final states. The sensitivity of the amplitude analysis, *i.e.* how small a signal can be detected, depends on having sufficient statistics and how well systematics, both from the experiment and from the analysis, are controlled. GlueX collaborators have recently been awarded an NSF grant to develop tools for understanding the phenomenological systematics inherent in an amplitude analysis. To estimate the sensitivity we expect from GlueX requires a full simulation of the detector response to real and background events, charged particle and photon reconstruction, kinematic fitting to identify exclusive final states and finally the actual amplitude analysis. Work is in progress on all of these, but the complete study has not yet been completed. In the following, we perform a comparison of what has been done in a successful spectroscopy experiment (Brookhaven E852) and what is expected in GlueX.

The E852 experiment used an 18 GeV/c π^- beam incident on a hydrogen target. The detector is a spectrometer based on a dipole magnet that produced nearly-uniform 1 T magnetic field over a volume that was 1.8 m wide (in the bend plane), 1.2 m high and 4.6 m long (along the beam line). E852 also had a calorimeter downstream of the dipole for detecting photons. GlueX has about one-half the beam energy as E852, and uses a 4 m long, 2.25 T solenoidal field for tracking charged particles. GlueX has both a downstream calorimeter and a second calorimeter in the barrel region. While E852 has very good momentum resolution for forward-going charged particles, it was unable to reconstruct recoil protons from the target. GlueX has reduced tracking resolutions for the forward going particles, but better acceptance for recoil protons. GlueX also has a larger calorimeter coverage than E852. While a system-by-system comparison of the two detectors is interesting, the true measure of their abilities comes from reconstructed spectra that are related to the underlying physics. In the following, we present these comparisons (as taken from reference [20]).

3.1 A signature reaction: $\gamma p \to 3\pi p$

Recently a high-statistics study of the reactions

$$\begin{aligned} \pi^- p &\to p\pi^+\pi^-\pi^- \\ \pi^- p &\to p\pi^-\pi^0\pi^0 \end{aligned}$$

was performed using data from E852 [21]. The corresponding reaction of interest in GlueX is

$$\gamma p \to n\pi^+\pi^+\pi^- .$$

Using the underlying physics observed in E852, Monte Carlo events were generated for GlueX. Equal numbers of events corresponding to $\gamma p \to a_2^+(1320)n$ and $\gamma p \to \pi_2^+(1670)n$ were generated followed by the decays $a_2 \to \rho\pi \to 2\pi^+\pi^-$ and $\pi_2 \to f_2\pi \to 2\pi^+\pi^-$. This approximates the mass distributions observed in the E852 experiment for $\pi^- p \to 2\pi^-\pi^+ p$ at an incident momentum of 18 GeV/c. For the Monte Carlo sample we assume a photon beam energy of 9 GeV. The $|t|$ distribution followed a form $e^{-5\cdot|t|}$ and all the resonances have uniform angular decay distributions. In the E852 study of this reaction [21], the presence of a proton charged track is required in the trigger, but the momentum of the proton is not measured. The distributions in $|t|$, the 3π mass, the like-sign 2π mass and $\pi^+\pi^-$ mass for our Monte Carlo sample and for acceptance-uncorrected

E852 data are shown in Figure 2. For the GlueX events, the momenta and angles of the generated events were smeared according to parameterized resolution functions[1] [22]. The distributions for both GlueX and E852 are quite comparable.

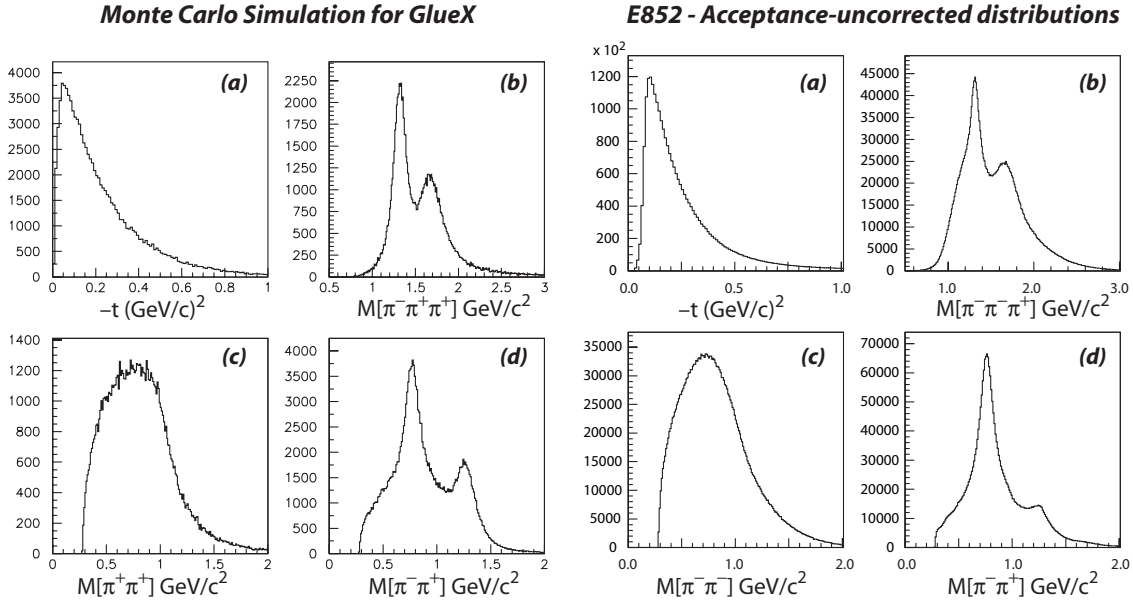

Figure 2: Physics distributions for the 3π final state. The left-hand plots are for simulated GlueX $\pi^+\pi^+\pi^-$ data while the right-hand plots are for E852 [21] $\pi^-\pi^-\pi^+$ data (plot taken from reference [20]).

For both the GlueX simulation and the E852 data, information about the nucleon recoiling against the 3π system is not used in kinematically identifying the event. Thus, a comparison of the missing mass is of interest. The missing mass squared distribution for the GlueX Monte Carlo sample is shown in Figure 3 along with a Gaussian fit (solid line). The σ for the Gaussian fit is 0.27 $(\mathrm{GeV/c^2})^2$. The corresponding E852 missing mass squared distribution had a σ of 0.31 $(\mathrm{GeV/c^2})^2$.

How do GlueX and E852 compare? The resolutions obtained for the π^0 mass resolutions for GlueX calorimetry are similar to those obtained in E852. Studies have been done to estimate the charged particle momentum and angle resolutions. The $\pi^-\pi^-\pi^+$ and $\pi^-\pi^+$ effective mass distributions and the distribution in the momentum transfer from the incoming beam to the outgoing 3π system observed in E852 were used to generate a Monte Carlo event sample of a similar final state for 9 GeV photoproduction. Charged particle momenta and angles were smeared using current best-estimate resolution functions and the result was that the resolution in the square of the missing-mass recoiling against the 3π system for GlueX will be at least as good as that in E852. This would indicate that the ability to kinematically identify exclusive reactions should also be at least as good.

[1]The parameterizations were based on resolution studies carried out using a detector model from 2007. It does not include the reduction of material in the FDC and CDC and the other design changes that have occurred since then. However, studies show that this is a good approximation to what would be expected using the current resolutions.

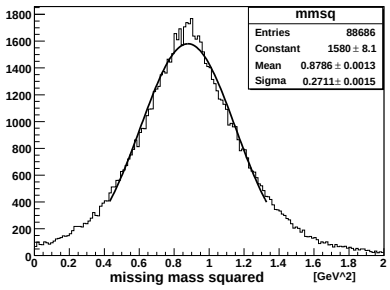

Figure 3: Distribution in missing mass squared recoiling against the 3π system for the Monte Carlo sample after resolution smearing. The distribution is centered at m_n^2 and the σ for the Gaussian fit (solid curve) is 0.27 $(\mathrm{GeV/c^2})^2$. The corresponding E852 missing mass squared distribution had a σ of 0.31 $(\mathrm{GeV/c^2})^2$(plot taken from reference [20]).

3.2 Expectations for amplitude analysis

With the previous comparison, we can turn to results of analysis from experiment E852 at Brookhaven. Data were collected from $\pi^- p$ interactions at 18 GeV/c leading to the final states $\pi^-\pi^0\pi^0 p$ and $\pi^-\pi^-\pi^+ p$ [21]. That experiment used the multiparticle spectrometer (MPS) at the AGS. Figure 4 shows the results of an amplitude analysis for the $J^{PC} = 2^{++}$ and $J^{PC} = 4^{++}\rho\pi$ amplitudes. Two well-established meson states are observed in these amplitudes, the tensor state $a_2(1320)$ in the former and the spin-4 state $a_4(2040)$ in the latter. The intensity of the a_4 is about 3% that of the a_2 and the amplitude of the a_4 is similar for the $\pi^-\pi^0\pi^0$ and $\pi^-\pi^-\pi^+$ systems, even though the experimental systematics for these two modes are very different.

Given the success of E852 in extracting a small signal, we expect that GlueX should be able to reach the same level of sensitivity. In photoproduction, the a_2 production cross section is about 0.5 μb, for a similar statistics data set to E852, a 15 nb cross section should be observable in GlueX and with the expected higher statistics, this lower limit could be even smaller.

3.3 Other mass distributions

3.3.1 K_S^0 events

Another signature GlueX reaction which has been studied [23] is:

$$\gamma p \to K^{*+}(890)K^{*-}(890)p \to K_S^0\pi^+ K_S^0\pi^- p$$

where $K_S^0 \to \pi^+\pi^-$ so the final state has $3\pi^+3\pi^-$. The $K^{*+}(890)K^{*-}(890)$ are decay products of X whose mass is chosen uniformly between 2.0 and 2.5 GeV/c^2 and is produced with a $|t|$ dependence $\propto e^{-5\cdot|t|}$. The $K\pi K\pi p$ resulting from $K^{*+}(890)K^{*-}(890)p$ is kinematically similar to other intermediate states leading to $K\pi K\pi p$ and to what is generated by PYTHIA. This channel has important discovery potential for exotic $s\bar{s}$ hybrids.

The momentum and lab angle spectra and their correlation for the K_S^0 are shown in Figure 5. The momenta and angles of all charged tracks were smeared to follow the estimates of the resolution in momentum (p), polar angle (θ) and azimuthal angle (ϕ) as functions of these variables. Figure 5(d) shows the distribution in all $\pi^+\pi^-$ effective mass combinations for nominal resolutions (solid) and for the case when the momentum resolution is degraded by a factor of two.

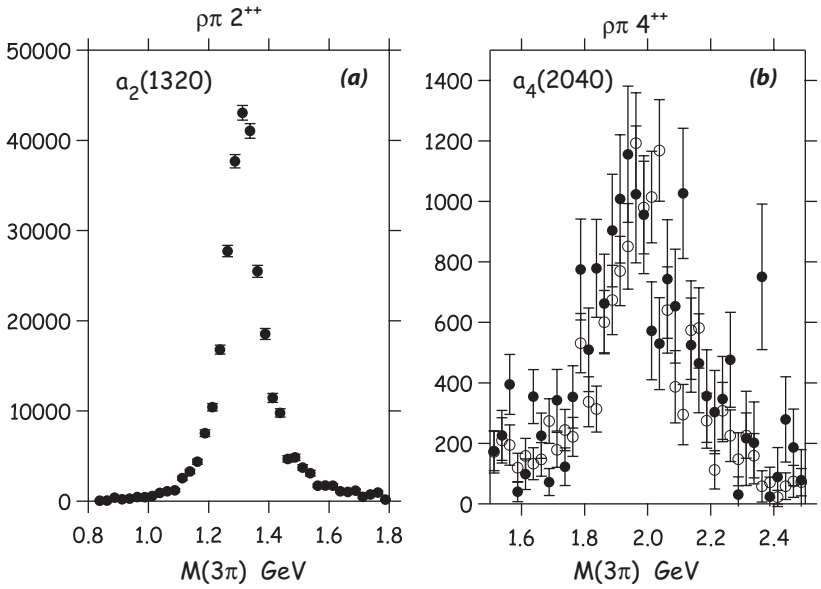

Figure 4: (a) Results of an amplitude analysis of data from $\pi^- p$ interactions at 18 GeV/c leading to the final states $\pi^-\pi^0\pi^0 p$ and $\pi^-\pi^-\pi^+ p$ from Brookhaven experiment E852 [21]. Results are shown for the (a) $J^{PC} = 2^{++}$ and (b) $J^{PC} = 4^{++}\rho\pi$ amplitudes. Filled circles are for the $\pi^-\pi^0\pi^0$ system and unfilled for the $\pi^-\pi^-\pi^+$ system. In (a) the tensor state $a_2(1320)$ is observed and in (b) the well-established spin-4 $a_4(2040)$ is seen. Note that the intensity of the a_4 is about 3% that of the a_2.

As a check of uniformity, the correlation plot of Figure 5(a) is divided into four regions, of roughly equal population, as shown where the dividing lines are at a momentum of 2.5 GeV and at an angle of 10°. Table 7 shows the K^0_S mass resolution for these regions under two assumptions about the momentum resolution. The nominal mass resolutions for a narrow state like the K_S are

Region	Nominal Resolution	Degraded Resolution
I	7.4 ± 0.2 MeV	13.8 ± 0.3 MeV
II	9.4 ± 0.2 MeV	16.6 ± 0.3 MeV
III	7.2 ± 0.2 MeV	13.2 ± 0.3 MeV
IV	5.9 ± 0.2 MeV	10.8 ± 0.3 MeV

Table 7: K^0_S mass resolutions assuming nominal tracking resolution and for the momentum resolution degraded by a factor of two (resolutions come from [22]). The regions refer to those in Figure 5(a) (table taken from reference [23]).

very good and reasonably uniform over the detector acceptance.

3.3.2 Mass resolutions involving charged particles and photons

Many of the expected decay modes of exotic hybrids involve narrow daughter products such as η, ω and ϕ. To compare the contributions of charged particle resolution and photon resolutions to

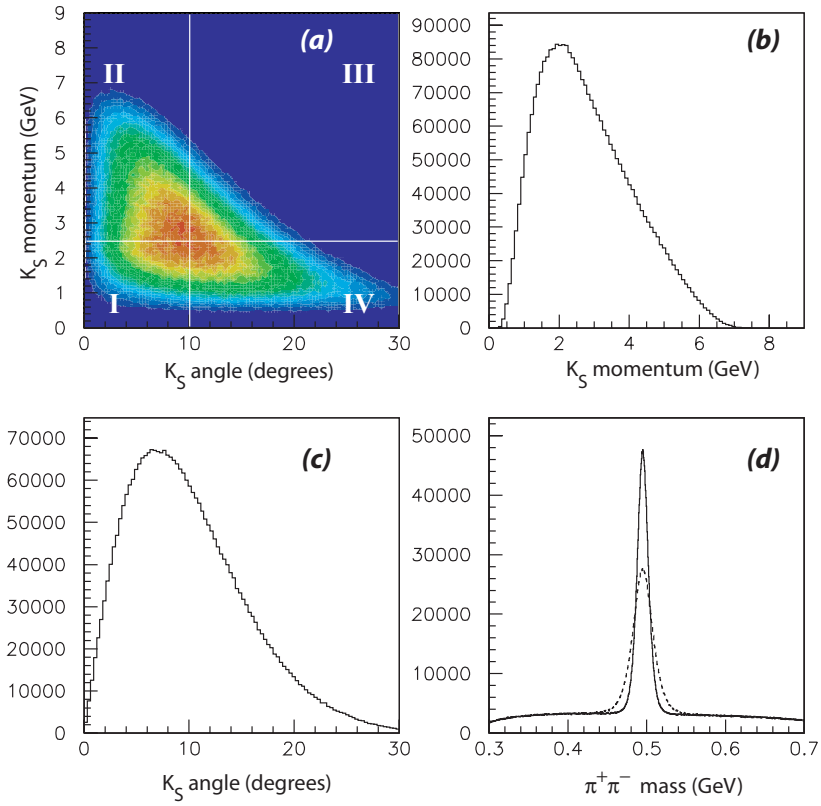

Figure 5: Kinematics of the K^0_S for the reaction $\gamma p \rightarrow K^0_S \pi^+ K^0_S \pi^- p$. Please see text for details (figure taken from reference [23]).

narrow width particles, as in the decays $\eta \rightarrow \pi^+\pi^-\pi^0$, $\omega \rightarrow \pi^+\pi^-\pi^0$ and $\phi \rightarrow \pi^+\pi^-\pi^0$, we studied the reaction $\gamma p \rightarrow \phi p$ [1]. For this study, the distribution in $|t|$ followed $e^{-|t|/2}$ to provide a mix of charged particle momenta that would include more lower momentum particles. The ϕ was generated with a mass and width of 1020 and 4 MeV/c^2 respectively. The charged particle four vectors (for the $\pi^{\pm}$) were smeared to follow the momentum error and angular error plots generated in a study of track finding in GlueX [22]. The plots shown in the referenced study were fit to analytical forms. These plots were generated before the material associated with the CDC and FDC tracking chambers was reduced so the nominal charged particle resolutions are somewhat over estimated. The study also considered what would happen if the nominal charged particle resolutions improved by a factor of two. The effect of the resolution smearing on the observed width of the ϕ is shown in Table 8. The distribution in the square of the missing mass recoiling against the ϕ is shown in Figure 6 under the same assumptions of four-vector smearing. The nominal errors associated with the charged particles are very similar to those for the π° in both of these cases.

3.4 Kinematic fitting of exclusive final states

GlueX will measure exclusive final states in order to carry out amplitude analysis. This means that physics constraints such as energy and momentum conservation, as well as the masses of particles that decay to photons can be used to constrain and improve the measurements of particle

Condition	Nominal errors for $\pi^{\pm}$	Nominal errors/2 for $\pi^{\pm}$
Photon smearing only	14.8 ± 0.1 MeV/c^2	14.8 ± 0.1 MeV/c^2
Charged particle smearing only	16.7 ± 0.1 MeV/c^2	11.1 ± 0.1 MeV/c^2
Both smeared	22.2 ± 0.2 MeV/c^2	17.6 ± 0.1 MeV/c^2

Table 8: Observed width for the ϕ, generated with a width of 4 MeV/c^2, after four-vector smearing.

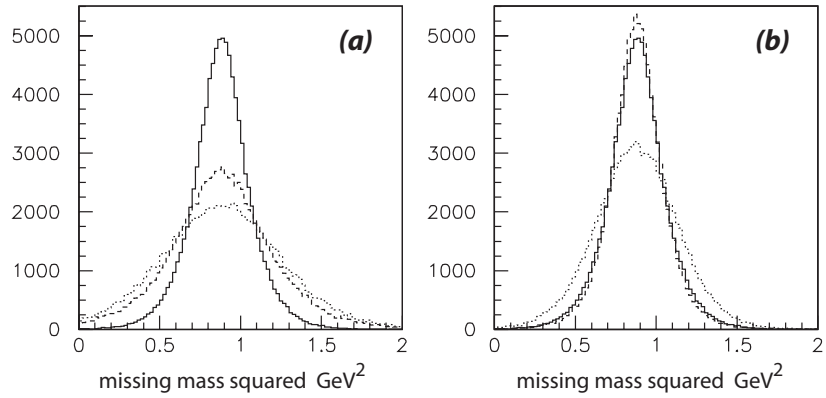

Figure 6: Missing mass squared recoiling off the ϕ for the reaction $\gamma p \to \phi p$ with photon smearing only (solid histogram), charged particle smearing only (dashed) and both (light dashed) for nominal charged particle smearing (a) and smearing reduced by a factor of two (b) (figure taken from reference [1]).

momentum and energy. The technique for doing this is known as kinematic fitting [24]. In order to show the effects of kinematic fitting in GlueX, we have examined reactions involving ω mesons decaying to $\pi^+\pi^-\pi^\circ$. For simple photoproduction of the ω meson, we have

$$\gamma p \quad \to p\omega \quad \to p\pi^+\pi^-\pi^\circ \, .$$

In this reaction, we assume that the π° is completely missing. The π° four-momentum is initially computed via energy and momentum conservation, and then the invariant mass of the three pion system is computed. This is shown in the left-hand plot in Figure 7, where we observe a mass resolution of about 0.32 GeV/c^2. Next, we perform a 1-constraint fit to the hypothesis of a missing π°. The right-hand plot of Figure 7 shows the resulting invariant mass after the fit. In this particular situation, the fit has improved the mass resolution by a factor of two.

In a related reaction, we consider

$$\gamma p \quad \to p\pi^+\pi^-\omega \quad \to p\pi^+\pi^-\pi^+\pi^-\pi^\circ \, .$$

Here, the additional pions produce a combinatorial background that makes it more difficult to identify the ω. Performing the same analysis, treating the π° as missing, and then computing all the neutral three-pion mass combinations, we go from the prefit distribution shown on the left of Figure 8 to the fit distribution on the right. Again, we see the resolution improving by about a factor of two with a significant reduction in the combinatorial backgrounds.

The one-constraint fits shown here are examples of the least constrained fitting that can be done in GlueX. In the same reaction, with the π° measured and the nucleon missing, we have a

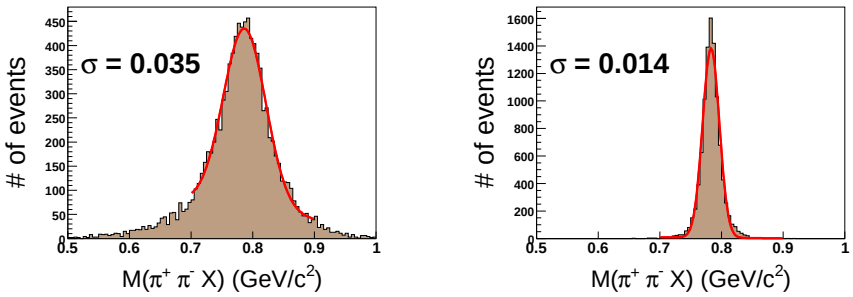

Figure 7: The reaction $\gamma p \to p\omega$. (left) is the 3π invariant mass before kinematic fitting, (right) is the same distribution after a 1-constraint fit to a missing π° is performed (See text for details.).

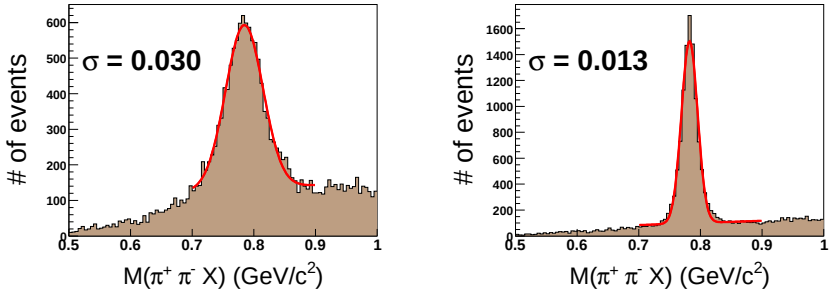

Figure 8: The reaction $\gamma p \to p\pi^+\pi^-\omega$. (left) is the 3π invariant mass before kinematic fitting, (right) is the same distribution after a 1-constraint fit to a missing π° is performed (see text for details).

second constraint, the mass of the π°. In the case where all particles are detected, the fit would have five constraints. As the number of constraints goes up, the ability to separate reactions with kinematic fitting improves. As with most other spectroscopy experiments, kinematic fitting will be an important analysis tool for GlueX.

4 Reconstruction of photons in GlueX

As discussed in section 2.4, nearly all of the photoproduction events observed in GlueX will have neutral particles (π^0 or η), which in turn come from the decay of heavier particles (see Table 3. The dominant source of photons in GlueX is the decay of π°s, followed by the two-photon decay of the η. Other reactions, such as radiative decays or direct photon production, contribute at a much smaller level. In GlueX, the resulting photons are detected by two calorimeter systems. A Lead-glass calorimeter in the forward direction (FCAL) and a Lead-scintillating fiber calorimeter inside the bore of the magnet (BCAL) (see Figure 1 for a schematic of the GlueX detector). Photons with polar angles between 1° and 10.8° (in the lab) will be detected and measured by the FCAL. Photons whose angles lie within the range of 10.8° to 126.4° will be detected and measured by the BCAL, while photons whose angles are greater than 126.4° or less than 1° will be undetected.

The FCAL [25] will be built using lead glass blocks that were used in both the e852 [26, 27] and RadPhi [28, 29] experiments. The design follows the granularity in those experiments using glass blocks with transverse dimensions of 4×4 cm^2 and xx cm long . These dimensions are a good match to the Molière radius (4.3 cm) of the lead glass. Approximately 2800 blocks will be stacked in a roughly circular wall with a 3 block by 3 block hole left around the beam line. The blocks will be viewed with photomultiplier tubes which will be read out using custom 250 MHz Flash ADCs [30].

The BCAL [31] is based on the KLOE calorimeter [32, 33] and consists of 23 layers scintillating fibers sandwiched between lead sheets. It will be 390 cm long and will and 22.5 cm thick. The calorimeter will viewed using a combination of silicon photo multipliers [34] and field-resistant photo multipliers. The signals will then be read out using a combination of 250 MHz Flash ADCs for energy information and TDCs for timing.

4.1 Energy and mass resolutions

4.1.1 Photon energy and position resolutions

The ability to efficiently reconstruct π^0 and η mesons is what drives the requirements on photon energy and position resolutions, and determine the mass resolutions of the π^0 and η masses. The energy resolution of calorimeters are typically parameterized as in equation 1 where the two constants, a and b, represent the *statistical* and *floor* contributions respectively.

$$\frac{\sigma_E}{E} = \frac{a}{\sqrt{\mathrm{E(GeV)}}} \oplus b \tag{1}$$

For the BCAL, we use $a = 0.054$ GeV$^{-1/2}$ and $b = 0.01$. These values come from detailed GEANT simulations [35], which are consistent with resolutions obtained with the KLOE calorimeter [32, 33] and with the beam tests of a BCAL 4-m module prototype [36]. For the FCAL, we use $a = 0.073$ GeV$^{-1/2}$ and $b = 0.036$ which have been obtained for the RadPhi calorimeter [28, 29].

The position resolution in $R\phi$ of the BCAL can be parameterized using equation 2 where R is the BCAL inner radius (65 cm) and ϕ is the azimuthal angle.

$$\delta(R\phi) = \frac{5 \text{ mm}}{\sqrt{\mathrm{E(GeV)}}} \tag{2}$$

This is consistent with results of BCAL simulations [35] and with the planned 2×2 cm^2 readout scheme (for the inner part of the barrel) for the ends of the BCAL modules. The polar angle, θ,

resolution is assumed to be driven by the resolution in z along the BCAL fiber which in turn is driven by the resolution in time difference between the two ends of a BCAL module. For the timing resolution, we use the expression given in equation 3 (where the times are all in ps).

$$\sigma_t(\text{ps}) = \frac{54}{\sqrt{\text{E(GeV)}}} \oplus 50 \tag{3}$$

From the above timing resolution, the resolution in z is given by

$$dz = \frac{1}{2}\sigma_t \cdot v_{eff} \tag{4}$$

where v_{eff} is the effective velocity of light in the fibers that takes into account the index of refraction and bounces ($v_{eff} = 0.53c$). From this, the resolution in polar angle (σ_θ is given as in equation —refeq:bcaltheta.

$$\sigma_\theta = \frac{R}{R^2 + z^2} dz \tag{5}$$

Figure 9 shows the dependence of σ_θ as a function of θ for various photon energies.

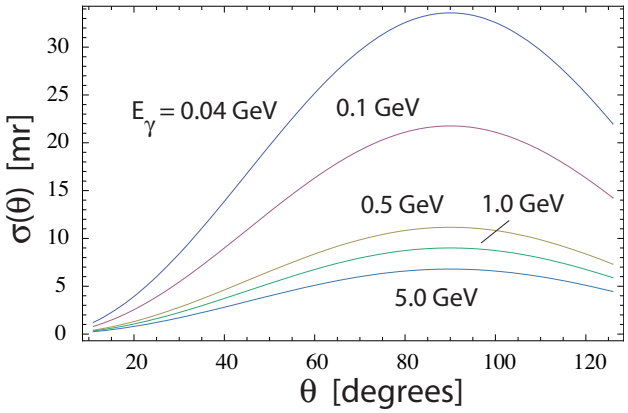

Figure 9: BCAL polar angular resolution as a function of angle for photon energies of 0.04, 0.1, 0.5 and 1.0 GeV.

For FCAL we take the position resolution in the plane of FCAL to be that measured in RadPhi [28].

$$\sigma_r = \frac{6.4 \text{ mm}}{\sqrt{\text{E(GeV)}}} \tag{6}$$

4.1.2 Mass resolutions

Given the energy an position resolutions in section 4.1.1, we look at the di-photon masses for the photons originating from the decays of π^0s and ηs. To examine this, we generated events corresponding to the reaction $\gamma p \rightarrow \eta\pi^0 p \rightarrow 4\gamma p$ at $E_\gamma = 9$ GeV, with $\eta\pi^0$ mass distribution uniform in mass from 1 to 2 GeV/c^2 and uniform in angles with $t-$dependent production of $e^{-5\cdot|t|}$. The photon energies and positions are smeared and compute the di-photon masses.

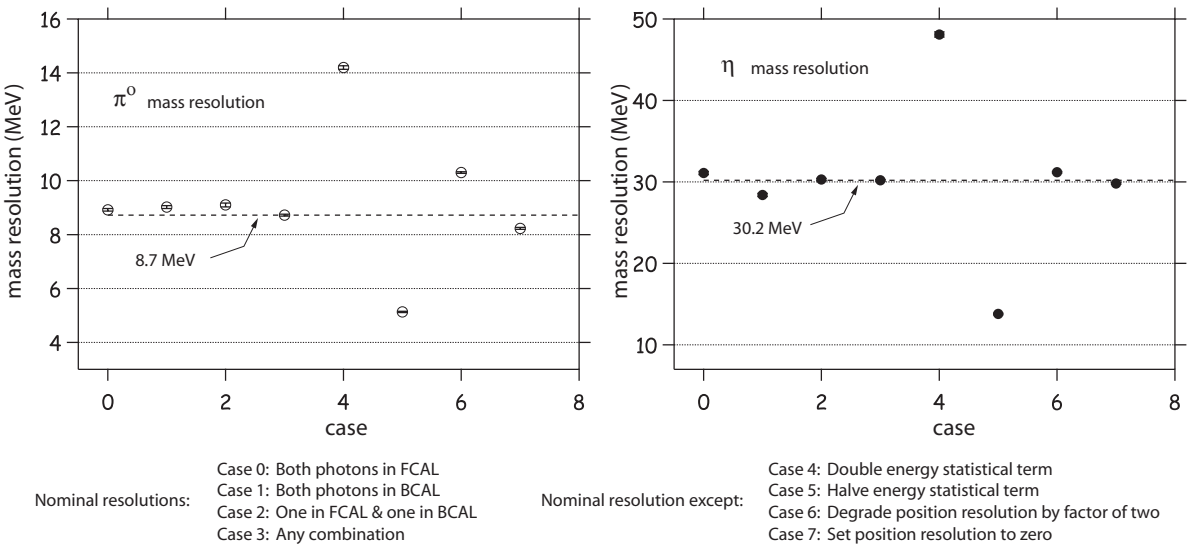

Figure 10: The π^0 and η mass resolutions obtained under different assumptions for energy and position resolutions in FCAL and BCAL.

The resulting distributions are fit to a Gaussian and the widths obtained from these fits are plotted in Figure 10. Because the photons are detected in two calorimeter systems, we need to consider several different detection geometries. These different cases are numbered 0 through 7 and correspond to the horizontal axis in Figure 10. The cases considered are: (0) when both photons from the η or π^0 are in FCAL; (1) when both photons are in BCAL; (2) when one photon is in BCAL and the other in FCAL; and (3) any combination of FCAL/BCAL. We also considered, for any combination, degrading or improving the nominal resolution. These cases are: (4) doubling the statistical term in the energy resolution; (5) halving the statistical term in the energy resolution; (6) degrading the position resolution by a factor of two and (7) assuming perfect position determination. The mass resolutions for the η and π^0 are 30.2 MeV/c^2 and 8.7 MeV/c^2 respectively. By comparison the η and π^0 widths were measured as 30.8 ± 0.5 MeV/c^2 and 12.1 ± 0.1 MeV/c^2 respectively in E852 for the reaction $\pi^- p \to \eta\pi^0 n$ [37]. The mass resolution is primarily driven by the energy resolution and the mass resolution of the π^0 is more sensitive to the position resolution compared to the η.

Figure 11 shows the di-photon mass for the $\eta\pi^0$ reaction with six entries per event after resolution smearing assuming nominal resolutions and degrading and improving the energy resolution by a factor of two. Also shown are the results of fitting the spectrum near the η mass region to a sum of a Gaussian and linear background. Both signal and combinatoric background are integrated over $\pm 2\sigma$ to obtain an estimate of signal (S) over combinatoric background (N). In this study the combinatoric background in the four-photon sample comes from $\eta\pi^0$ events. The four-photon sample will also be populated by $\pi^0\pi^0$ events which will increase the combinatoric background depending on the relative cross-sections for these two final states. Kinematic fitting can be used to eliminate the $\pi^0\pi^0$ events from the four photon sample. This technique was used in the E852 experiment to study $\eta\pi^0$ final state [38] which has a cross-section about an order of magnitude lower than for the $\pi^0\pi^0$ final state in π-induced interactions. Another source feeding the four-photon sample will be final states with more than four photons where one of the photons is undetected or final states with

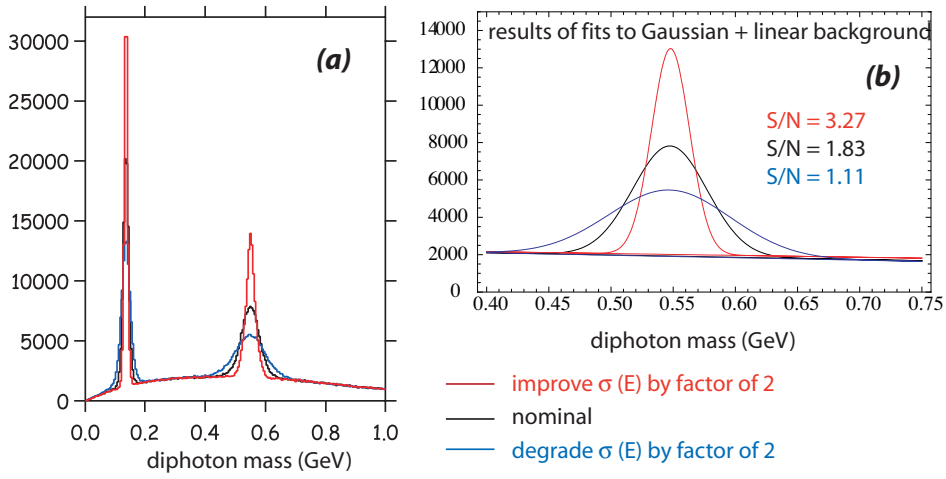

Figure 11: (a) The di-photon mass for the $\eta\pi^0$ reaction after resolution smearing using nominal resolutions (black), improving σ_E by a factor of two (red) and degrading σ_E by a factor of two (blue). There are six combinations per event. (b) Results of fitting the η mass region with a Gaussian and linear background. The background and signal were integrated over $\pm 2\sigma$ to obtain signal over noise S/N for the three resolution assumptions.

fewer than four photons but with spurious additional photons either resulting from interactions in detector material or due to an artifact of the reconstruction software.

4.2 Kinematics for reactions of interest in GlueX

We now use our tuned version of PYTHIA (Section 2.5) to provide estimates of the multiplicity of photons in the GLUEX calorimeters along with their energies and angles. Figure 12 shows photon information for 1 M PYTHIA events. About 78% of the events have at least one photon leading to a 3.2 M photon sample. The photon multiplicity is shown in Figure 12(a) The correlation of photon energy with angle is shown for all photons in BCAL (Figure 12(b)), in FCAL (Figure 12(c)) and for photons with angles greater than 126° (Figure 12(d)). The percentage of all photons entering FCAL is 27.3%, entering BCAL is 70.5%, with angles greater than 126° is 1.7% and entering the beam hole in FCAL (defined by angles less than 1°) is 0.5%. So BCAL and FCAL together will be illuminated by about 98% of all photons with BCAL having about 2.5 times more photons than FCAL. The implications of not detecting the 1.7% of photons that have angles greater than 126° will be discussed in section 4.3.4.

An important parameter for either calorimeter is the energy threshold. Table 9 shows the fraction (in percent) of events with more than one photon in a calorimeter for which the minimum energy in the event is less than the threshold energy. These are percentages obtained by averaging over all topologies (charged and neutral particles). As will be seen in section 4.3.3, for some signature reactions in GLUEX involving multiple photons and charged particles, the overall event acceptance will depend critically on the minimum energy at which a photon can be reconstructed.

The plots of Figure 13 address the issue of the granularity needed for the BCAL. Distributions for (a) photon multiplicity in BCAL for events with one or more photons in BCAL; (b) separation of photons in azimuthal angle for photons in BCAL (multiple entries per event); and (c) minimum

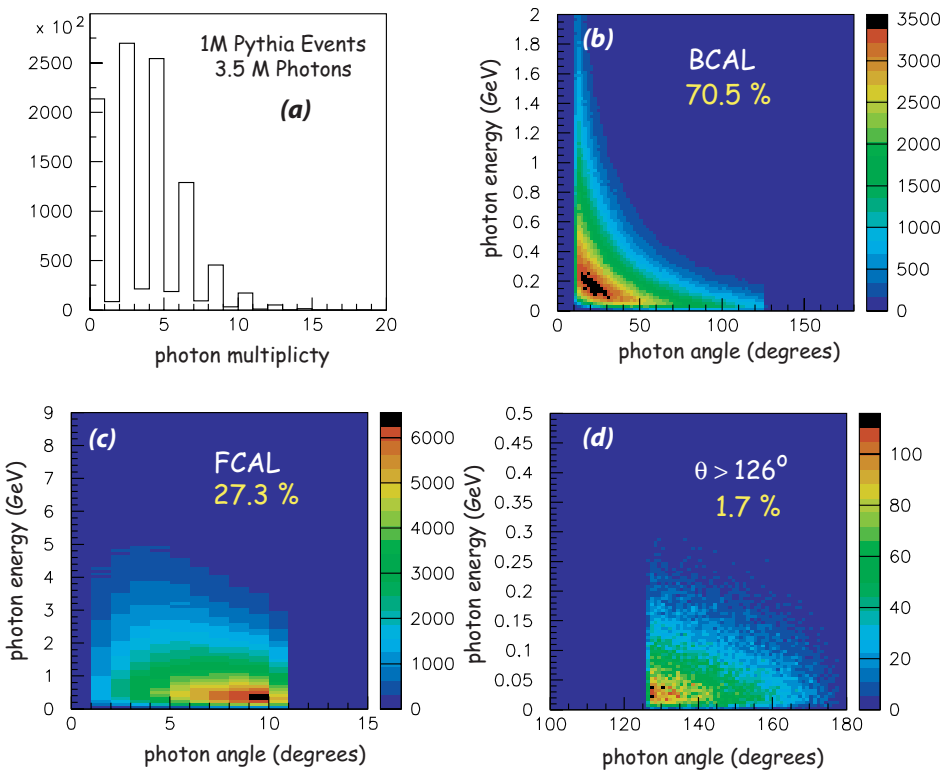

Figure 12: (a) Photon multiplicity for 1M PYTHIA events. About 78% of the events have at least one photon leading to a 3.2 M photon sample. The correlation of photon energy with angle is shown for photons in (b) BCAL, (c) FCAL and (d) for photons with angles greater than 126°. Note that the plot axes have different scales.

azimuthal angle separation in an event are shown. Also shown is the correlation of azimuthal separation (all di-photon combinations in an event) with photon multiplicity. The BCAL readout cell size is approximately 2×2 cm^2. The in depth (along the radius) the segmentation is exactly 2 cm and along the azimuth the width varies with depth to correspond to an azimuthal segmentation of 1.875°. This segmentation is for the first 12 cm in depth but it accounts for providing the bulk of information needed for photon reconstruction. The segmentation for the remaining depth has a coarser segmentation. This cell size is a good match to the BCAL Molière radius (3.6 cm). Approximately 6% of events with two or more photons in BCAL have a photon pair with an azimuthal angular separation less than 2°.

The plots of Figure 14 address the issue of the granularity needed for FCAL. Distributions for (a) photon multiplicity in FCAL for events with one or more photons in FCAL; (b) photon distance from center of FCAL in the plane of FCAL; and (c) photon separation in the plane of FCAL (multiple entries per event) are displayed. Also shown is the (d) (x,y) pattern of photon hits on the plane of FCAL.

The granularity of the FCAL follows the design used in E852 [26, 27] and RADPHI [28, 29] based on glass blocks with transverse dimensions of 4×4 cm^3. These dimensions are a good match to the Molière radius (4.3 cm) of the lead glass that will be used in FCAL. Simulations using PYTHIA events show that for all the events with two or more photons in FCAL, 0.7% of these events have a

Energy Threshold E_{thr} (MeV)	BCAL: % with $E_{min} < E_{thr}$	FCAL: % with $E_{min} < E_{thr}$
20	2	0
40	5	0.1
50	8	0.2
100	17	1.9
150	25	4.8

Table 9: Fraction (in percent) of events with more than one photon in a calorimeter for which the minimum energy in an event is less than the threshold energy.

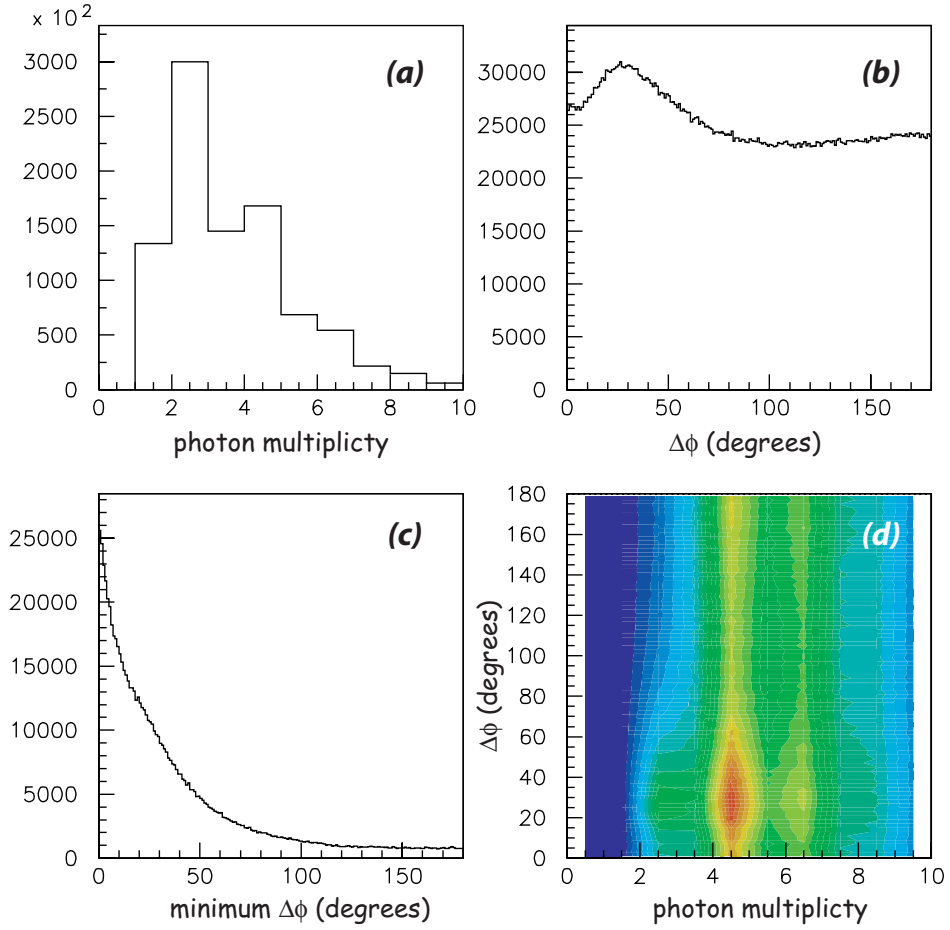

Figure 13: Photons in BCAL: distributions in (a) photon multiplicity in BCAL for events with one or more photons in BCAL; (b) separation of photons in azimuthal angle for photons in BCAL (multiple entries per event); (c) minimum azimuthal angle separation in an event; (d) correlation of azimuthal separation (all di-photon combinations in an event) with photon multiplicity.

minimum di-photon separation of 8 cm or less. The minimum photon separation can be computed

from 7

$$\Delta r = \frac{2m_\pi L_{FCAL}}{E_\pi^{max}} \tag{7}$$

where L_{FCAL} is the distance from the target (560 cm) and $E_\pi^{\max}$ is the maximum pion energy. The maximum energy π^0 (E_π^{max}) expected for GlueX is 9 GeV for nominal running with polarized photons and 12 GeV for photon running near the electron endpoint energy. This corresponds to a minimum di-photon separation of 16 and 13 cm for the two energies.

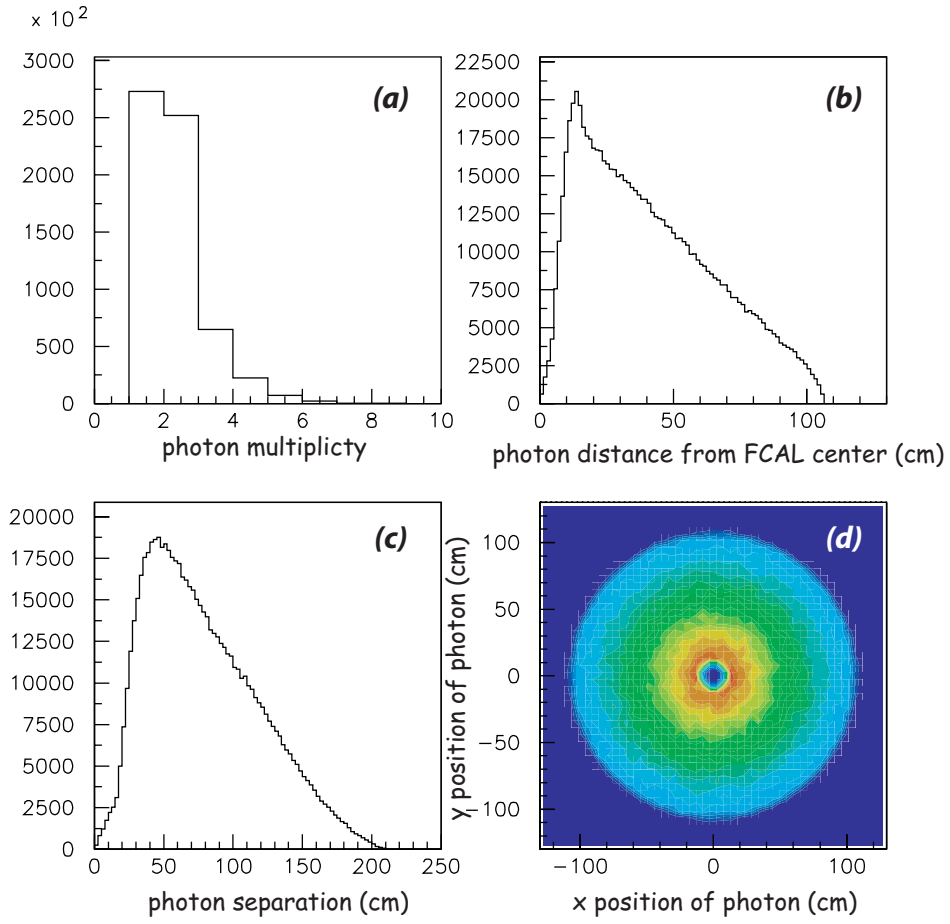

Figure 14: Photons in FCAL: distributions in (a) photon multiplicity in FCAL for events with one or more photons in FCAL; (b) photon distance from center of FCAL in the plane of FCAL; (c) photon separation in the plane of FCAL (multiple entries per event); and (d) (x,y) pattern of photon hits on the plane of FCAL.

4.3 Photon acceptance in GlueX

To understand the acceptance for photons in GlueX, we return to the $\gamma p \to \eta\pi^0 p$ reaction from section 4.1.2. This reaction is of particular interest for exotic hybrid searches since the $\eta\pi^0$ has well-defined charge conjugation quantum number ($C = +$) and if the η and π^0 resonate in a $P - wave$ then the resonance has exotic $J^{PC} = 1^{-+}$. For events with uniform $\eta\pi^0$ masses between 1.0 and

2.0 GeV/c^2, uniform in decay angles, and produced with a $e^{-5\cdot|t|}$ distribution, the photons populate the calorimeters, the beam hole in FCAL and the angular region $> 126°$ as shown in Table 10. For completeness we include the photon population for PYTHIA events and for events with recoil baryon resonance production $\gamma p \to X\Delta \to X\pi^0 N$. The latter reaction will be discussed in more detail below.

Table 11 shows the fraction of accepted (no photons in beam hole or with angles $> 126°$) events that have both photons from the η or π^0 in FCAL or BCAL or shared between FCAL and BCAL.

Element	Percent of all photons PYTHIA Events	Percent of all photons $\eta\pi^0$ Events	Percent of all photons $X\Delta$ Events
Angles $> 126°$	1.7	0.20	7.8
BCAL	70.5	45.68	89.8
FCAL	27.3	53.15	2.4
Hole in FCAL	0.5	0.97	0

Table 10: Fraction of all photons populating the GLUEX calorimeters, the angular region $> 126°$ and the beam hole in FCAL for PYTHIA events and $\eta\pi^0$ events.

Element	η	π^0
Both photons in FCAL	27%	46%
Both photons in BCAL	20%	35%
Photons in FCAL and BCAL	53%	19%

Table 11: Fraction of accepted $\eta\pi^0$ events that have photons from either the η or π^0 both in BCAL or FCAL or shared.

Figure 15 has information about the photons hitting BCAL. The variable z is the distance along the inner surface of BCAL starting from the upstream end at $z = 17$ cm and ending at the downstream end at $z = 407$ cm. The 30-cm target center is at $z = 65$ cm. The histogram is the distribution of the photons along z (use the left vertical scale) while the dashed curve (use the right vertical scale) is the integral fraction of photons in percent. For example, 30% of the BCAL photons hit between $z = 17$ cm and $z = 212$ cm, the upstream half of BCAL. The other curves also use the right vertical scale. The green curve is the number of BCAL radiation lengths intercepted by the photon trajectory assuming a 1.45 cm radiation length for the Pb/SciFi matrix. The cusp at $z = 312$ cm corresponds to a photon angle of 14.7° where the number of radiation lengths is 68. As the photon angle changes from 10.8° to 14.7°, the number of radiation lengths intercepted by the photon trajectory increases from 0 to 68. In this angular region the photon trajectory exits out the downstream end of BCAL. The cusp at $z = 30$ cm corresponds to a photon angle of 118.1°. The minimum of the green curve is at $z = 65$ cm or at 90° corresponding to 17 radiation lengths (the module is 22.5 cm thick). The blue curve shows the photon angle as a function of z.

4.3.1 Photons near the downstream end of the BCAL

As seen in Figure 15, the angular region between 10.8° and 14.7° has a significant population of photons for events of the reaction $\gamma p \to Xp \to \eta\pi^0 p$. This region not only abuts the gap between the BCAL and the FCAL, but also is shadowed by material associated with other detectors. In the

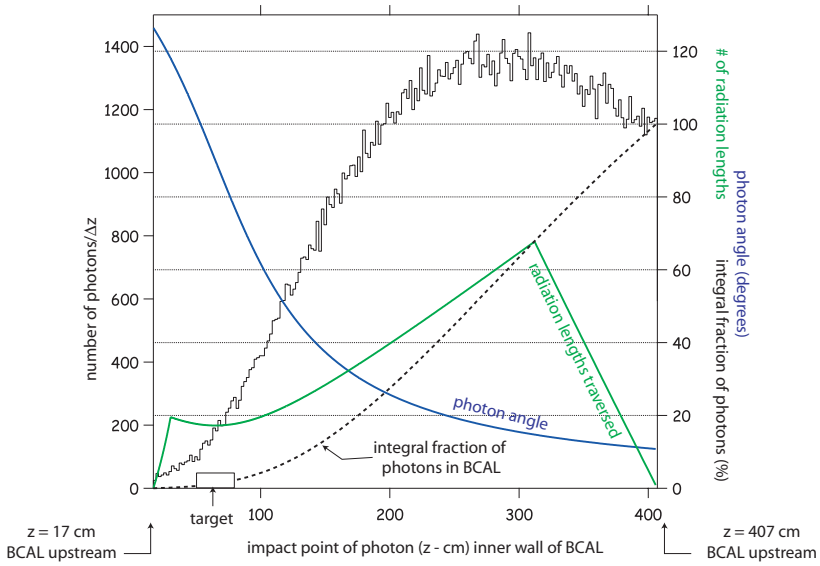

Figure 15: Histogram: Distribution of photons from the $\gamma p \to \eta\pi^0 p$ reaction along the inner wall of BCAL. The upstream end of BCAL is at $z = 17$ cm and the downstream end at $z = 407$ cm. Use the left vertical scale for the histogram. The three curves (all as a function of z) use the right vertical scale. The black dashed curve is the integral fraction of photons in BCAL in percent. The blue curve is the photon angle in degrees measured with respect to the beam (or with respect to the inner surface of BCAL). The green curve is the number of radiation lengths traversed by a photon.

original design there was a fair amount of material due to cabling associated with the FDC drift chambers in this region. Recent design changes have resulted in a significant reduction of material. The results of these changes are shown in Figure 16. The curve labeled "March 2007" corresponds to the original design, that labeled "March 2008" is the result of changes to the frames of the FDC packages and moving the most down stream package away from this region. The "No FDC Cable" curve is the result of removing the FDC readout cables from the region. The result of these changes in the design is that the gap between the two calorimeters is only about 0.5° in size.

4.3.2 The impact on amplitude analysis

How well one understands the reconstruction efficiency in this region is critical for the amplitude analysis. To illustrate this, we generate events with a uniform population of decay angles in the X rest frame. A frame that is often chosen is the Gottfried-Jackson frame where the polar angle, θ_{GJ}, is the angle between the momentum vector of one of the decay products (the η in our case) and the momentum vector of the beam, all in the X rest frame. A uniform decay angular distribution corresponds to a distribution flat in $\cos\theta_{GJ}$. The amplitude analysis fits the observed distribution in $\cos\theta_{GJ}$ to a sum of various waves corresponding to the angular momentum L between the η and π^0 and its projection M along the $z-$axis.

In Figure 17 we show the effect on the $\cos\theta_{GJ}$ distribution where we eliminate $\eta\pi^0$ events if one of the four photons from the event enters an angular region defined by the LAB angle θ. For distribution (I) no requirement was imposed. For distribution (II) the angular cut imposed extends from $\theta = 10.8°$ to $\theta = 11.7°$. For distributions (III) through (V), the lower limit remained the

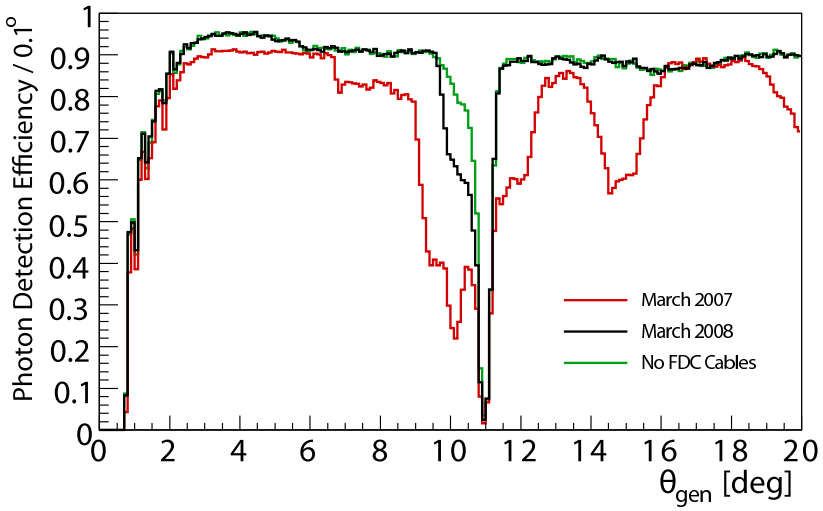

Figure 16: Results of optimization of material in front of the gap between the BCAL and the FCAL in GlueX. The curve labeled 2007 had the most down stream FDC package shadowing the gap, as well as the cables for the FDC routed through the gap. The curve labeled 2008 has the FDC moved up stream such that it no longer shadows the gap, but the FDC cables are routed through the gap. The curve labeled "No FDC Cables" has is the same as 2008, except the FDC cables are routed to the up stream end of the detector and do not go through the gap.

same while the upper limit was increased in 1° increments, up to $\theta = 14.7°$ for distribution (V). We currently believe that GlueX should be between curves I and II. Also shown are the percentage of events that survive the various angular cuts along with the forward-backward asymmetry defined as $(F - B/(F + B)$ where F is the number of events with $\cos\theta_{GJ} > 0$ and B is the number of events with $\cos\theta_{GJ} < 0$. The imposition of the angular cut impacts the acceptance and sculpts the observed angular distribution. As noted above, if the $\eta\pi^0$ resonates in a P-wave ($L = 1$) the resonance has exotic quantum numbers. There are resonances with $L = 0$ and $L = 2$ that decay into $\eta\pi^0$ and an even-wave odd-wave interference will lead to a forward-backward asymmetry in the $\cos\theta_{GJ}$ distribution. So a poorly understood acceptance in the critical angular region between BCAL and FCAL can lead to false amplitude analysis conclusions.

4.3.3 Low energy photons

An important parameter for BCAL is the energy of the lowest energy photon that can be reconstructed. To understand the challenge we look at another reaction of interest in exotic hybrid searches: $\gamma p \to b_1^+\pi^0 n$. For this reaction, the intermediate final state is $\omega\pi^+\pi^0$ and the final state is $\pi^+\pi^+\pi^-\pi^0\pi^0 n$. Here we look at the kinematics for a 2 GeV/c^2 state decaying into $b_1\pi$ (expected for an exotic hybrid). The incident photon energy is assumed to be 9 GeV.

The plot of Figure 18(a) shows the energy spectrum of the lowest energy photon in the event. The plot of Figure 18(b) shows the fractional running integral, so, for example, 25% of the events have a photon with energy less than 80 MeV. The scatter plot of Figure 19 shows the energy versus angle for the lowest energy photon in the event for $\gamma p \to b_1^+\pi^0 n$. This scatter plot shows the challenge for this lowest energy photon reconstruction. Most of the low energy photons occur near

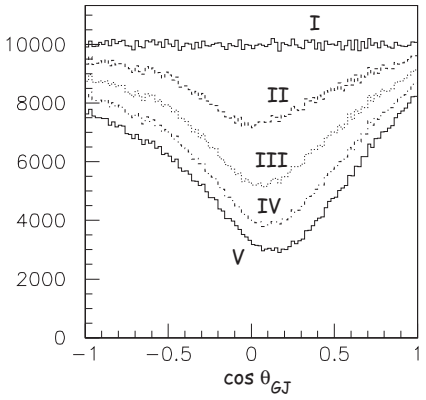

Case	Acceptance (%)	(F-B)/(F+B)
I	100	0.0
II	85	-0.01
III	73	-0.03
IV	63	-0.06
V	55	-0.08

Figure 17: The distribution in $\cos\theta_{GJ}$ for $\gamma p \to Xp \to \eta\pi^0 p$ events. For distribution (I) no cuts are imposed. For distributions (II) through (V), events are eliminated if one of the four photons enters various angular ranges as defined in the text. The corresponding acceptances and forward-backward asymmetries are also given.

the edge of BCAL where reconstruction is a challenge due to presence of material at that location.

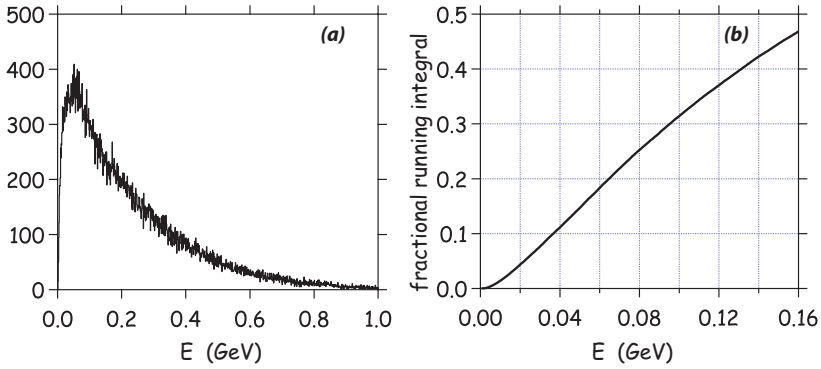

Figure 18: Left: Spectrum of lowest energy photon in a $\gamma p \to b_1^+\pi^0 n$ event; Right: Fractional running integral for the plot to the left.

4.3.4 Photon coverage at large angles

As noted in Figure 1, there is no photon detection for photons with angles $> 126^\circ$ and from Table 10 we see that the percentage of all photons for PYTHIA events and for $\eta\pi^0$ events that populate this angular range is small. The class of photoproduction reactions that populate this angular region with photons are reactions resulting in the production of a forward meson (X) and a recoil excited baryon decaying into $\pi^0 p$ or $\pi^0 n$. Since the application of the amplitude analysis depends on identification of exclusive final states, it will be important to identify such reactions by explicitly measuring the decay products of the baryon resonance or to veto events offline that have a extraneous π^0 or photons too low in energy to be identified kinematically given the limitations on resolution in missing mass.

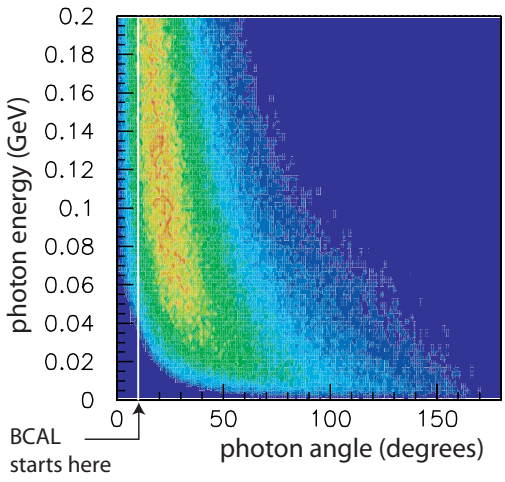

Figure 19: Energy versus angle for the lowest energy photon in the event for $\gamma p \to b_1^+ \pi^0 n$.

To understand the effect of the presence of baryon resonances we generated $\gamma p \to X\Delta$ events where X is a resonance of mass uniformly distributed between 1.0 and 2.0 GeV/c^2 and produced with a distribution in momentum transfer squared (t) given by $e^{-5\cdot|t|}$. The Δ mass and width are 1.236 and 0.15 GeV/c^2 respectively and the decay mode is $\pi^0 N$. The kinematics of the recoil baryon is determined by the value of $|t|$ and is independent of M_X expect for the dependence of $|t|_{min}$ on M_X. The percent of all photons generated that populate various angular regions is summarized in Table 10. The percentage of photons with angles $> 126°$ is relatively large but these events can be tagged for elimination by using information from FCAL and BCAL, but primarily the latter. For the sample generated, 80% of the events have both photons from the π^0 (the Δ decay product) in BCAL and 85% have both photons in either FCAL or BCAL or shared between the two. Only 0.3% of the events have no photons in either FCAL or BCAL so effectively more than 99% of the baryon resonance events can either be measured or tagged.

Extending the upstream end of BCAL by 30 cm would increase the backward angle coverage to 140° and would recover about 50% of the backwards-going photons that are now missed. Extending to 140° would recover 70% of the photons missed with the current configuration but would require adding and additional 67 cm to the calorimeter. The deterioration in BCAL performance by such modifications would not be justified by this additional photon coverage.

How large are these baryon resonance cross sections? The cross section measurements near GlueX energies show significant Δ^{++} production in the 3-prong and 5-prong topologies but little Δ^+ or Δ^0 production. For example, in the 3-prong topology, the cross sections for $\rho^-\Delta^{++}$, $\rho^0\Delta^+$ and $\rho^+\Delta^0$ are 1.1 ± 0.2 μb, 0.3 ± 0.2 μb and 0.2 ± 0.2 μb respectively. The cross sections for $n\rho^0\pi^+$ and $\Delta^-\pi^+\pi^+$ are 2.0 ± 0.6 μb and 0.2 ± 0.2 μb respectively [39]. In the 5-prong channel with a single π^0, reactions with a Δ^{++} account for nearly 75% of that channel but no reactions with Δ^+ are quoted. Although measurements are based on low statistics, there appears to be little Δ^+ or Δ^0 production.

4.4 Overall calorimeter performance of GlueX

This section has summarized the performance of the calorimeters in GlueX. The anticipated energy and position resolutions come from comparisons to existing detectors, prototypes and Monte Carlo simulation. These in turn lead to invariant mass resolutions for π° and ηs that are comparable to Brookhaven E852. We have also presented a careful summary on the impact of acceptance on our ability to do physics. This includes both physical gaps, as well as low-energy threshold effects. We end this section by returning to the $\gamma p \to p\eta\pi^\circ$ reaction and make a comparison between the overall acceptance of E852 to that of GlueX. The upper two plots in Figure 20 show the acceptance as a function of $\eta\pi^\circ$ mass for E852 and GlueX. While that for E852 falls rapidly with increasing mass, the acceptance of GlueXis both large and constant over the mass range of interest for GlueX. The lower plots show the acceptance in the Gottfried-Jackson frame for the $\eta\pi$ system. The acceptance of GlueX is both larger overall, more uniform than that in E852.

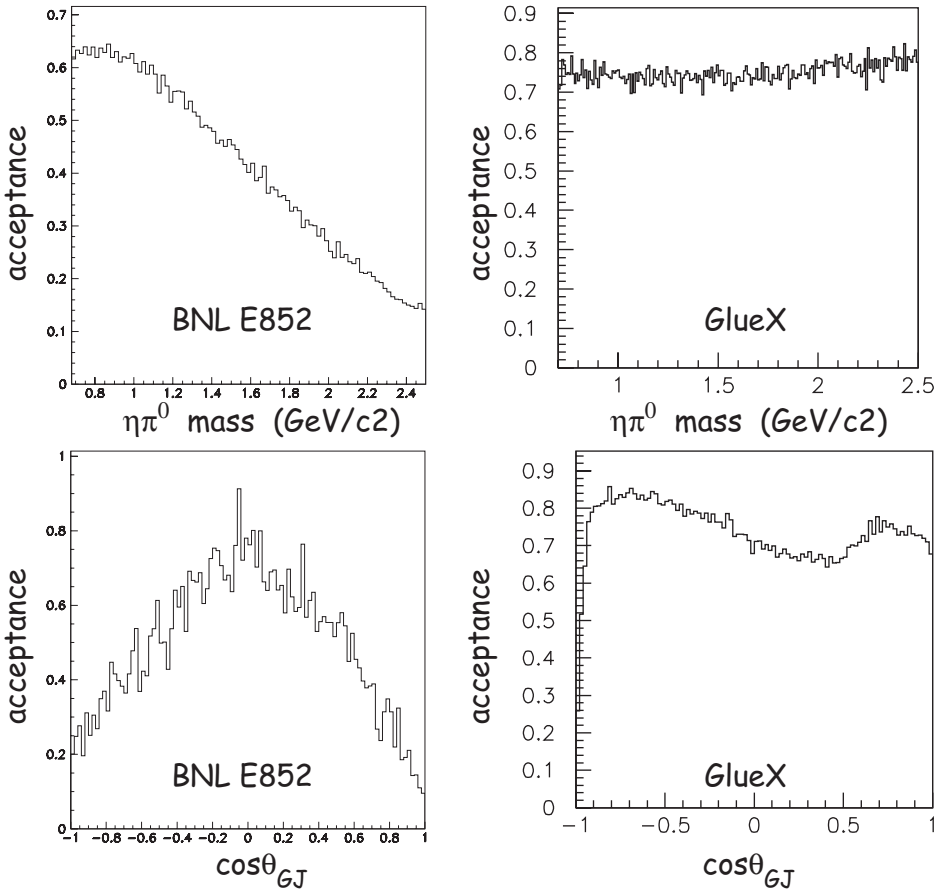

Figure 20: A comparison of the expected acceptance of the GlueX detector for the reaction $\gamma p \to p\eta\pi^0$ with the acceptance of the E852 experiment. The upper two plots show the acceptance as a function of the mass of the $\eta\pi$ system, while the lower two plots show the acceptance as a function of the Gottfried-Jackson angle.

5 Reconstruction of charged particles in GlueX

Charged particles ($\pi^{\pm}$, $K^{\pm}$ and p) will be reconstructed using two tracking systems. The CDC around the target and the FDC in the downstream half of magnet. The CDC [40] is a 24-layer, 1.5-m long straw tube chamber, while the FDC [41] packages are cathode-plane drift chambers. These are described in detail in the references. Here we only note that the CDC should achieve a 150 μm resolution normal to the wire. Using stereo layers, a z resolution along the wire of about ~ 1.5 mm can be achieved. The FDC will make measurements in the x-y plane (normal to the beam direction) with a resolution of 200 μm. Together, these detectors will track particles from threshold up to nearly 8 GeV/c. The kinematics of the photoproduction reaction tend to give the particles a forward boost with the highest momentum particles traveling at small angles and essentially being only detected in the FDC. Particles with larger transverse momentum tend to have lower overall momentum and will be tracked in some combination of the two chambers.

The angular regions of detection can roughly be divided as follows. Particles going more forward than about 1° in the lab will go down the beam line and not be detected by any tracking detector. Outside of this, to about 6°, particles will be tracked only in the FDC. From 6° out to 30°, particles can be detected by both the CDC and the FDC. Realistically, for both the CDC and the FDC to be used in reconstruction, the particles are in the range of about 8° to 24°. From 30° to about 150°, particles will be reconstructed in the CDC alone. In fact, hits will be observed in the CDC back to 168°, but the track resolution will be reduced due to the fact that the number of hits along a track will be fewer than 10. However, for the key physics program in GlueX, there will be essentially no particles at such large angles.

5.1 Momentum resolution

As discussed above, charged particles are reconstructed in the detector using the CDC and FDC. To determine the momentum resolution for charged particles in GlueX, the particles are tracked using the detector simulation package HDGEANT [42],[43] based on GEANT 3.14. This simulation contains our best estimate of all the material in GlueX, as well as models for all relevant detector responses. The resulting events are then reconstructed using the GlueX reconstruction software [22, 44]. The current software uses hits from the chambers with design resolutions to find, and then fit the tracks. Both the Monte Carlo and the reconstruction software use a realistic field map for the solenoidal magnetic field including fringe fields that extend out to the time-of-flight wall. The fit momentum is then compared with the generated momentum, which yields to the resolution plots shown in this section.

We start with the momentum resolution,

$$\sigma_{\Delta p/p} \;=\; \frac{\Delta \mid \vec{p} \mid}{\mid \vec{p} \mid} .$$

Figure 21 shows a plot of momentum resolution versus polar angle for several fixed values of total momentum in the range of 1 to 7 GeV/c. There are several structures seen in Figure 21 that can be understood in terms of the geometry of the detector. The degradation in resolution for very forward tracks is due to the small bending for these tracks, which go roughly parallel to the magnetic field in GlueX . The degradation that occurs in the angular range of 10° to 25° correspond to particles not hitting all the FDC packages (a jump is observed each time a package is not hit). The rise in the backwards direction corresponds to particles passing through the upstream endplate of the

CDC—however this structure is in a region of phase space that has no events. In fact, most of the angular region backwards of 40° will rarely have particles of momentum larger than 2 GeV/c. Most particles in this region will have a momentum resolution better than 1.5%.

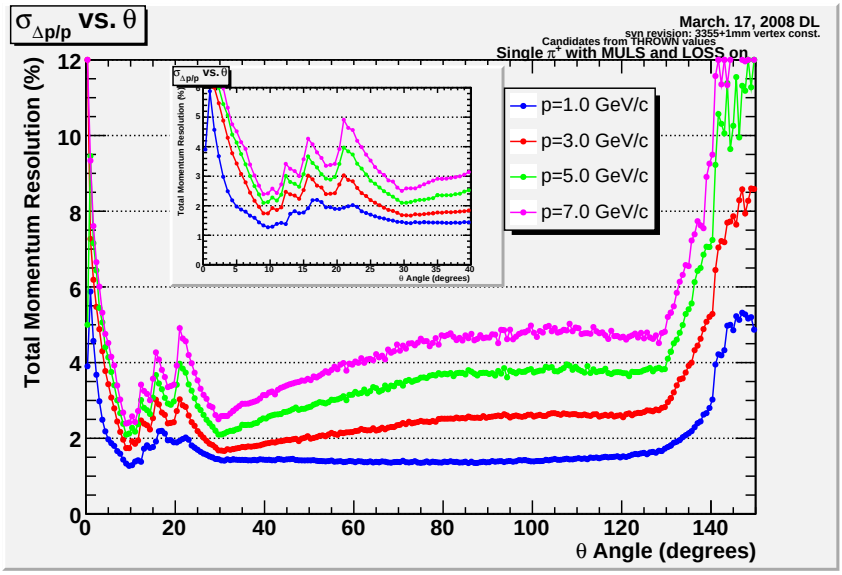

Figure 21: Momentum resolution (%) as a function of the polar angle θ at the primary vertex for several values of momentum p (figure taken from reference [44]).

We next look at the polar angle resolution,

$$\sigma_{\Delta\theta} \quad = \quad \Delta\theta\,.$$

Figure 22 shows the angular resolution for slices of polar angle θ going from 10° to 90°. Finally, the azimuthal angular resolution

$$\sigma_{\Delta\phi} \quad = \quad \Delta\phi$$

is shown in Figure 23.

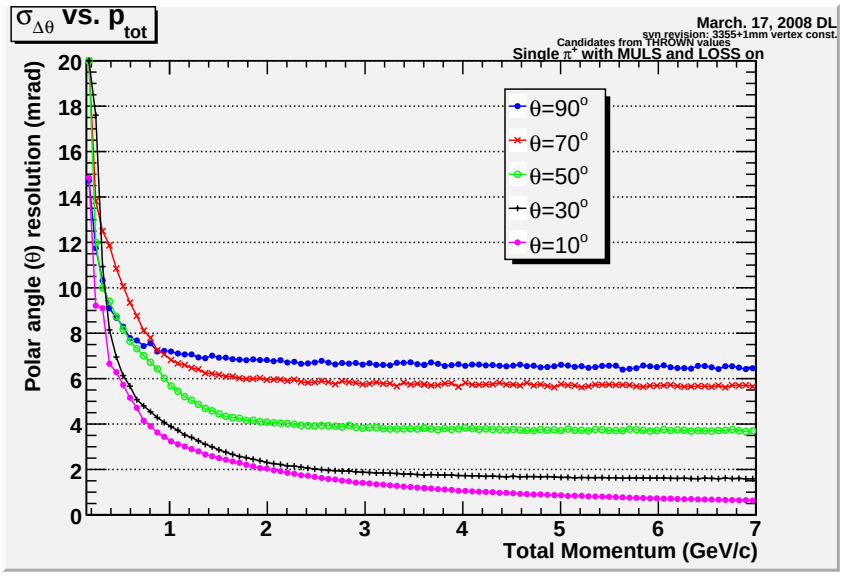

Figure 22: Polar angle resolution (mrad) as a function of the total momentum p for various polar angle θ at the primary vertex (figure taken from reference [44]).

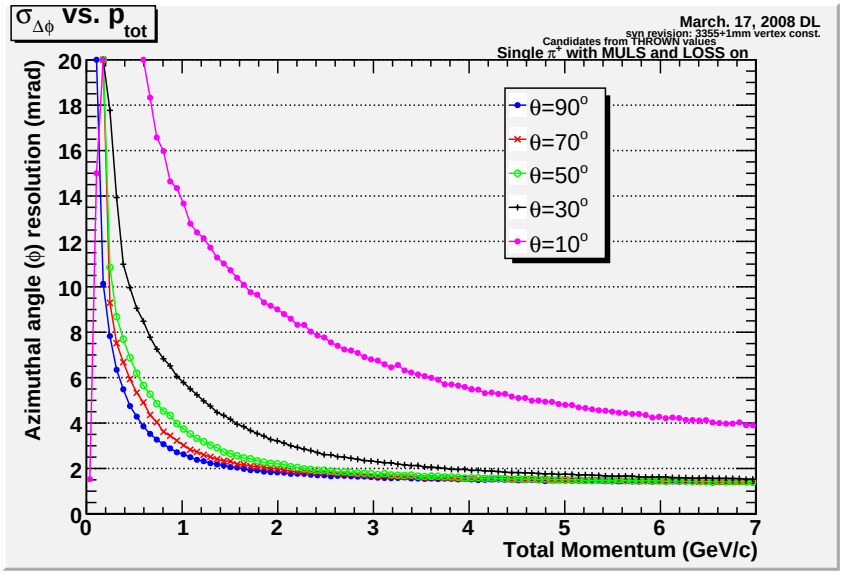

Figure 23: Polar angle resolution (mrad) as a function of the total momentum p for various polar angle θ at the primary vertex (figure taken from reference [44]).

5.2 Track finding and fitting

The current version of the GlueX reconstruction software starts with a track-finding package that looks for tracks in the CDC and FDC separately, and then tries to merge them. Figure 24 shows the track-finding efficiency for this package as a function of both total number of hits and which chambers the tracks are located. The solid triangles show the track finding efficiency as a function of the polar angle θ when only the FDC is used. The solid squares show the same plot for the CDC. The solid circles show the efficiency for finding either a CDC or FDC track. The colored regions labeled FDC and CDC map the number of hits on the track in the particular detector. Overall, there is good track-finding efficiency in GlueX with nearly 100% efficiency everywhere. Track-finding in the presence of electromagnetic backgrounds have also been studied in GlueX. These studies show a few percent, degradation of the efficiencies shown here [44].

After carrying out track finding, the tracks need to be fit to obtain particle information. A track fitting package has been developed, but as with track finding, developmental improvements will continue over the next five years. At present, the GlueX track fitter is not quite as efficient as track finding. The current losses appears to be related to pathologies in the fitting routines. Work on resolving these deficiencies is in progress, and it is anticipate that the GlueX track fitting efficiency will improve to more closely match that of track finding [44].

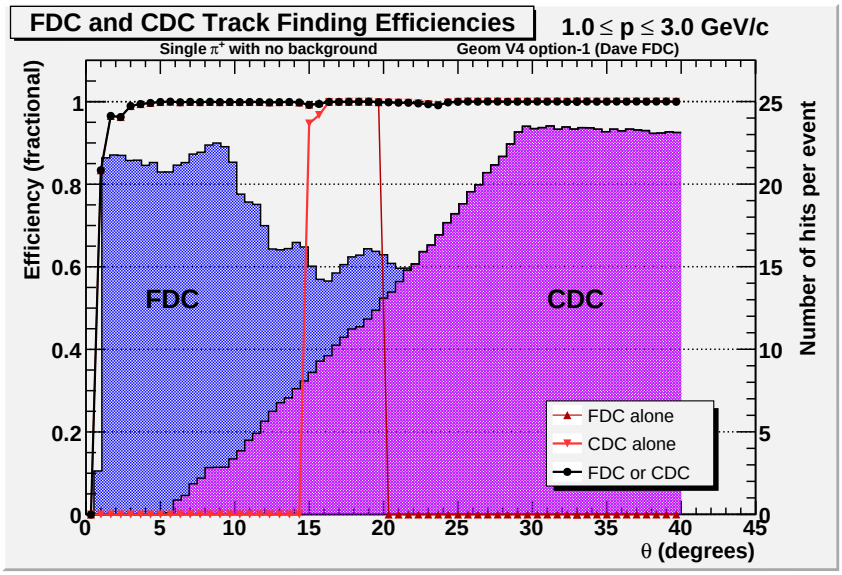

Figure 24: Track finding efficiency in the CDC and FDC, see text for explanation (figure taken from reference [44]).

Based on the resolutions obtained from HDGEANT and the GlueX reconstruction software, a set of parameterized resolution and acceptance functions have been developed. These functions provide a pseudo event reconstruction which can be used to carry out more sophisticated GlueX studies. An example of these studies are studies of effective and missing mass resolutions earlier in this report.

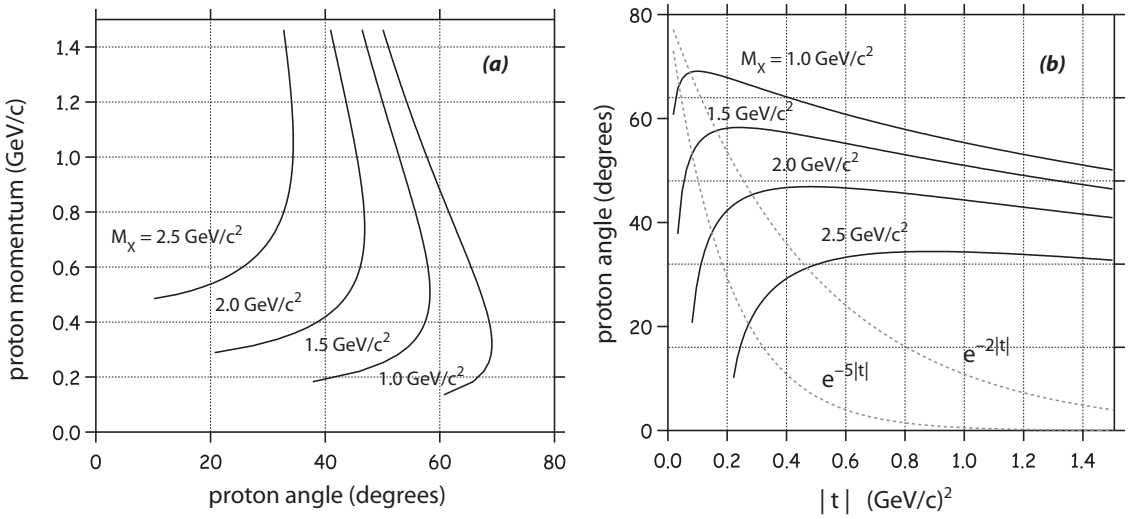

Figure 25: (a) Recoil proton LAB momentum as a function of proton LAB angle, measured with respect to the beam direction, for $\mid t \mid_{min} < 1.5$ (GeV/c)^2 for the reaction $\gamma p \to Xp$ for $M_X = 1.0, 1.5, 2.0$ and 2.5 GeV/c^2. (b) Recoil proton LAB angle, measured with respect to the beam direction as a function of $\mid t \mid$ for the reaction $\gamma p \to Xp$ for $M_X = 1.0, 1.5, 2.0$ and 2.5 GeV/c^2. Also shown are typical t distributions for $e^{-2|t|}$ and $e^{-5|t|}$ (light dotted curves) (figure taken from reference [45].

5.3 Kinematics for reactions of interest in GlueX

In order to understand how particles of various momenta populate the tracking elements, we need to consider some typical reactions that are part of the GlueX physics program [45]. The first of these is the generic reaction $\gamma p \to pX$, where X represents a mesonic system with mass less than 2.5 GeV/c^2. Such a reaction is expected to be produced in a t-channel process where the cross section has an exponential dependence on the magnitude of t, $e^{-\alpha|t|}$, with the slope, α varying from 2 to 5. Such a reaction defines the proton kinematics in the GlueX detector. Figure 25 shows the lab momentum and angles for protons produced in the reaction $\gamma p \to pX$ with X varying in mass from 1.0 to 2.5 GeV/c^2. Virtually all of these protons are detected in the forward half of the CDC, with many of them also tracked into the FDC packages. For $m_X = 2.5$ GeV/c^2, the most forward protons have a total momentum of about 0.4 GeV/c with this momentum becoming smaller as the mass of X gets smaller.

A signature reaction is $\gamma p \to n\pi^+\pi^+\pi^-$, where the 3π system has a mass in the range of 1.5 to 2.5 GeV/c^2. The distributions of charged pions from this reaction are shown in Figure 26. About 50% of these pions are only detected in the FDC. Most of the remainder pass through both the CDC and the FDC, with a tail of particles below about 1.5 GeV/c having hits only in the CDC. Other important reactions have larger numbers of pions, (4, 5, 6, ...). As the final state multiplicity becomes larger, the average particle momentum gets smaller, and slower particles are detected at larger angles in the CDC. For the reactions of interest for amplitude analysis, the detector acceptance is sufficient.

The hybrid strangeonium states are expected to decay predominantly through several final states that eventually populate the reaction $\gamma p \to pK^+K^-\pi\pi$ [46]. Within this final state, the

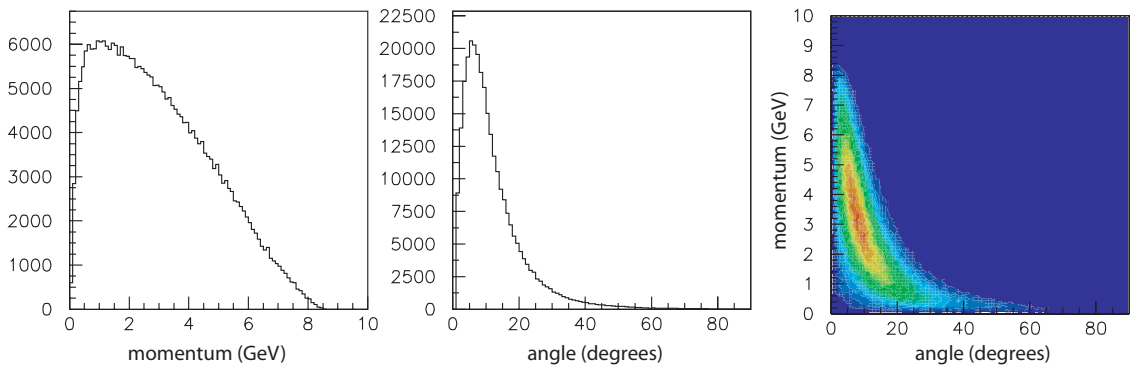

Figure 26: The momentum and angle spectra of charged pions and their correlation from the reaction $\gamma p \rightarrow \pi^+\pi^+\pi^- n$ for 8.5 to 9.0 GeV photons (figure taken from reference [45]).

following reactions are predicted by decay models to be the dominant decay modes.

$$\begin{aligned} \gamma p &\rightarrow pK_1^{\pm}(1410)K^{\mp} \\ \gamma p &\rightarrow pK_1^{\pm}(1270)K^{\mp} \\ \gamma p &\rightarrow pK^*(892)\bar{K}^*(892) \\ \gamma p &\rightarrow p\phi(1020)f_0(980) \end{aligned}$$

Assuming t-channel production, the distributions of kaon momentum versus angle are shown in Figure 27 for the four reactions above, where one assume a t slope of $\alpha = 5$ and a hybrid mass in the range of 2 to 2.5 GeV/c^2—in line with all current hybrid predictions [6]. These kaons tend to populate both the FDC and the forward part of the CDC and have momenta from several hundred MeV/c up to nearly 6 GeV/c, with the highest momentum tending to be in the very forward direction. In terms of the ability of GlueX to reconstruct charged particles, the distribution of physics events is a good match to the geometry of GlueX.

All of the reactions examined above tend to populate the GlueX tracking system with angles well forward of 90° in the lab. This is true for t-channel processes where a neutron or proton is connected to the lower vertex—the expected hybrid production mechanism. However, a competing reaction ($\gamma p \rightarrow \Delta X$) can generate both charged and neutral pions at more backwards angles. In this case, the pion from the decay of the Δ can be sent into the backwards direction. Because the CDC can reconstruct charged particles back to at least 150°, the detector will still have good acceptance for these more backwards pions.

5.4 Acceptance issues for charged particles

5.4.1 The Forward Hole:

The hole in acceptance in the very forward part GlueX has been defined by background rates in the FDC detectors. The rates at a given position along the beam line specify the minimum active radius of the FDC, with the radius becoming larger as one moves farther downstream. To make the hole uniform in all four FDC packages, the size is defined by tracking 1 GeV/c π^+ through the detector and taking the distance from the beam line in each of the four FDC packages. The result of this is shown in Figure 28. In particular, the first FDC package has a hole that is 2.3 cm in

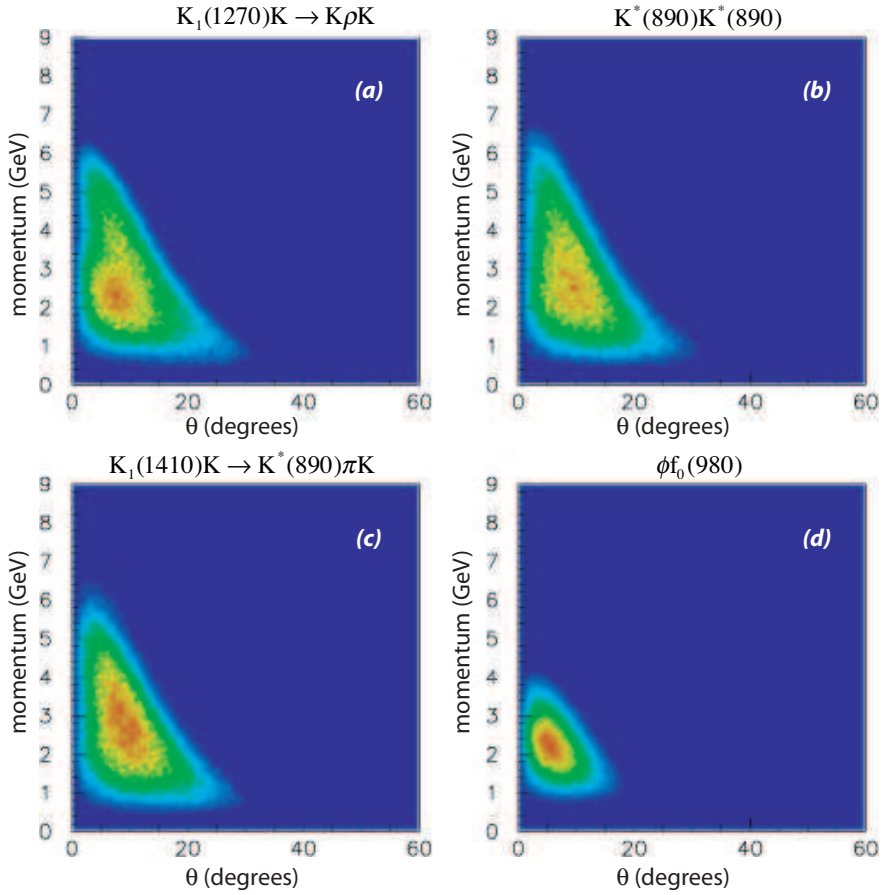

Figure 27: The momentum versus angle (in the lab) for $K^{\pm}$ in the reaction $\gamma p \to pK^+K^-\pi\pi$ for various intermediate states. (a) $K_1^{\pm}(1270)K^{\mp}p$; (b) $K^*(890)\bar{K}^*(890)$; (c) $K_1^{\pm}(1410)K^{\mp}p$; and (d) $\phi(1020)f_0(980)$ (figure taken from reference [45]).

radius and the fourth package has a hole that is 4.6 cm in radius, (note the mm label in the figure should be cm).

As can be seen in Figure 28, the angular size of the forward hole becomes somewhat smaller as the momentum is increased above 1 GeV/c and is larger for lower momenta. In particular, the curves that correspond to 0.25 GeV/c and 0.5 GeV/c show what appears to be an odd structure that is due to the helical trajectory in the magnetic field. Particles with 0.25 GeV/c momentum are tangentially approaching the beam axis in FDC packages two and three.

Because decays of hybrid mesons tend to have particles spread out over a large part of the GlueX detector, the effect of the hole in the forward direction will have very little impact on physics in GlueX. However, there are reactions where the physics can be impacted by the inability to detect forward-going particles. One particular reaction is diffractive ρ production.

There have been a number of studies of s-channel helicity conservation in diffractive vector meson production [13] [47]. Monitoring diffractive ρ production has been considered as a tool for monitoring the degree of linear polarization of the photon beam for GlueX. The helicity angles ($\cos\theta_H$ and ϕ_H) are the pion decay angles defined in the ρ rest frame, where the $\hat{z}$ is taken along

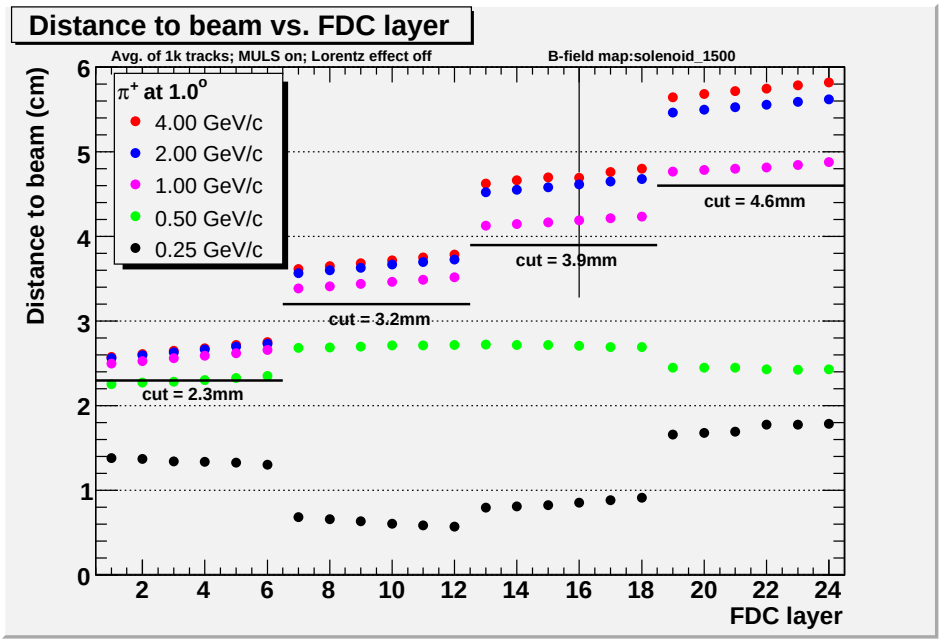

Figure 28: The forward hole near the beam line in the FDC is defined by the requirement that 1 GeV/c π^+ with $\theta = 1°$ will be measured in the FDC. The plots shows the maximum size of the hole around the beam line in each FDC package π^+ particles generated 1° with various values of momentum. The odd structure for 0.5 GeV/c and 0.25 GeV/c particles occurs due to spiraling of the tracks in the solenoidal field (figure taken from reference [44]). Note that the dimensions of the radial cuts should be labeled as cm and not mm.

the original ρ direction, $\hat{y}$ is normal to the ρ production plane, and $\hat{x} = \hat{y} \times \hat{z}$. A study of our ability to use this reaction to cross check our measurements of the photon polarization has been done.

In the study, events were generated assuming s-channel helicity conservation with a 40% linearly polarized beam at 9 GeV. The acceptance in the helicity angle distributions for a forward angle cut of 1° and 2° is shown in Figure 29. The distortion in the ψ_H distribution is severe, especially in going from the 1° cut to the 2°. Acceptance corrections can be made, but the knowledge of the efficiency and acceptance as a function of the angular cut have to very well understood to be able to use this as a monitoring tool. Cross checking the measured linear polarization using ρ decays may well be a challenge. However, because this reaction is very sensitive to how well the acceptance is understood, it will provide an excellent mechanism to test our understanding of the acceptance of GlueX, which in turn will improve our ability to do an amplitude analysis.

5.4.2 Low momentum cutoffs

Monte Carlo studies have been carried out to quantify the low-momentum thresholds for charged particles in GlueX. These cutoffs are dominated by energy loss in material before reaching the tracking volumes, as well as bending in the strong magnetic field. If we consider particles that traverse the CDC, the cutoff as a function of polar angle from 15° to 90° in the lab and momentum is shown in Figure 30. Pions with momenta smaller than about 0.15 GeV/c cannot be reconstructed in GlueX. For kaons, the cutoff is similar to pions at large angles, but rises to about 0.22 GeV/c

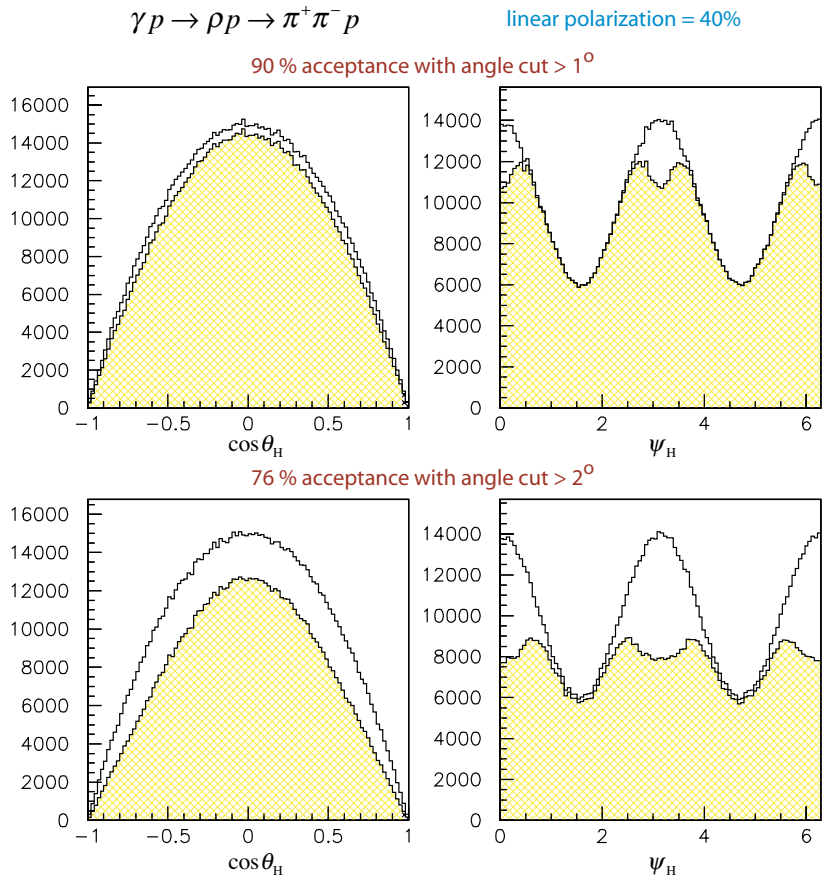

Figure 29: GlueX acceptance in the ρ helicity angles assuming 40% linear polarization for the photon beam. The top two plots are for a LAB angle cut of 1° and the bottom two for a LAB angle cut of 2° (figure taken from reference [44]).

for forward going Ks. For protons, the cutoff falls from about 0.33 GeV/c in the forward directions down to about 0.25 GeV/c at 90°. In terms of charged particle reconstruction, the efficiency for detecting slow protons has the biggest effect on the acceptance in GlueX. Combining this with the information in Figure 25, we see that for mesons systems (X) with masses below about 2 GeV/c^2, the low-t production will tend to produce a proton that will not be easily detected in GlueX. These protons will need to be reconstructed using kinematic fitting and missing mass techniques.

5.5 Overall performance of GlueX

The resolutions and efficiencies presented in this section ultimately come from a detailed GEANT Monte Carlo of GlueX and using realistic reconstruction software. These results have then been parameterized and used in section 3 to make comparisons to the performance of Brookhaven E852, an experiment that has carried out precision spectroscopy. It was shown that the performance of GlueX is comparable to those of E852 and thus, only using comparable statistics as E852, GlueX should be able to carry out physics analysis to at least the same level of precision.

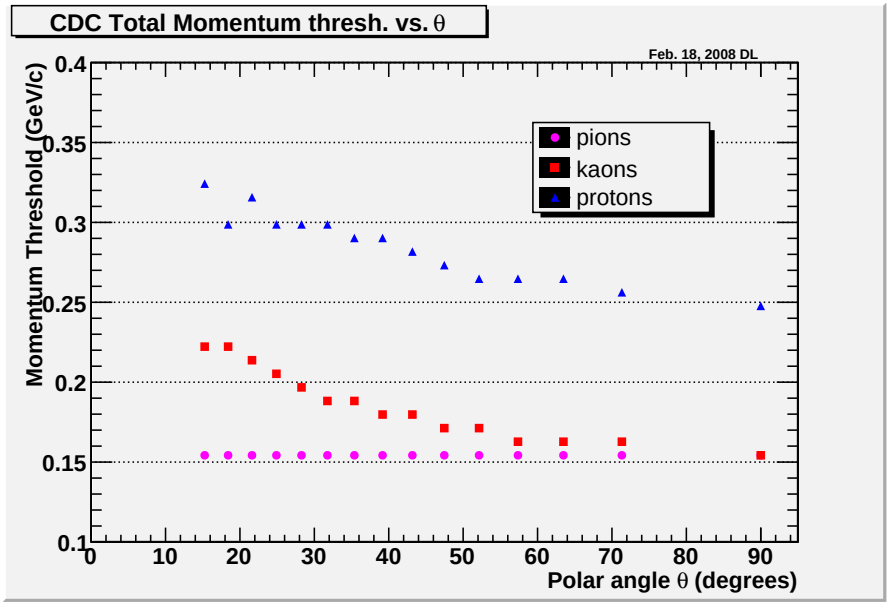

Figure 30: Momentum threshold for reconstructing charged particles in the CDC (figure taken from reference [44]).

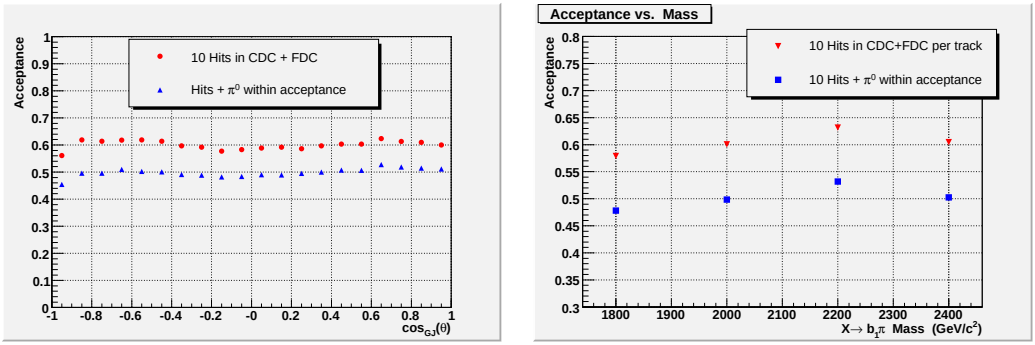

Figure 31: The acceptance of GlueX for the reaction $\gamma p \rightarrow n b_1(1235)\pi \rightarrow n\pi^+\pi^+\pi^-\pi^\circ\pi^\circ$. The left-hand figure shows the acceptance in the Gottfried-Jackson frame for a $b_1\pi$ mass of 2 GeV/c^2. The right-hand plot shows the acceptance as a function of the $b_1\pi$ mass.

6 Particle identification in GlueX

The lightest members of the spectrum of exotic hybrids will decay predominantly to final states that contain only pions and photons recoiling against either a proton or a neutron. For these particles, the ability to separate pions from protons (and exclude the much less common kaons) will be required. The GlueX detector has the ability to do this with several σ of separation, and this can be improved by adding kinematic fitting. Ultimately, GlueX also plans to search for the heavier $s\bar{s}$ hybrids, where one of the most promising decay modes involves two kaons and two pions. For these later searches, it will be necessary to also identify kaons. For this, the current ability of GlueX is not nearly as good, however this could be substantially improved with the addition of a Cherenkov detector in the forward direction. In addition to the hardware, we also anticipate sophisticated analysis that will look globally at an individual event to identify the best possible particle assignments consistent with all measured information.

In GlueX, the PID system consists of the forward TOF wall [48], time-of-flight in the BCAL and dE/dx information from the CDC. The TOF wall will measure flight times of charged particles in a roughly 11° degree wide cone about the beam axis with 80 ps accuracy. Additional information will come from time-of-flight measurements in the BCAL [31], which are expected to have an accuracy of 200 ps, and possibly from shower profile from charged particles in the BCAL. Finally, the CDC will measure dE/dx information that will be useful for particles below 0.45 GeV/c momentum. As discussed below, these systems will be able to separate pions from protons in GlueX. In addition, there will be kaon identification in a limited kinematic region.

6.1 Time of flight information

In GlueX, the reaction $\gamma p \to pK^+K^-\pi^+\pi^-$ (see Figure 27) is expected to be one of the best handles on the exotic $s\bar{s}$ states. Several reactions of interest follow the form:

$$\begin{aligned}
\gamma p &\to pX \to pK^*(890)K^*(890) \to pK^+K^-\pi^+\pi^- \\
\gamma p &\to pX \to pK_1(1410)K \to pK^+K^-\pi^+\pi^- \\
\gamma p &\to pX \to pK_1(1270)K \to pK^+K^-\pi^+\pi^- \\
\gamma p &\to pX \to p\phi(1020)f_0(980) \to pK^+K^-\pi^+\pi^- .
\end{aligned}$$

These reactions have been simulated [45] in the GlueX detector and the pions and kaons tracked to the BCAL or the TOF. Figure 32 shows the momentum spectrum of the pions and the kaons in both the BCAL and TOF for the first and last of the above reactions.

Roughly speaking, particles with a polar angle more forward than 11° will be detected in the TOF wall. With the detector located 5.53 m downstream of the target center, a good approximation for the pion/kaon time difference as a function of momentum is

$$\Delta t = \frac{L}{c}\frac{\sqrt{p^2+m_K^2}-\sqrt{p^2+m_\pi^2}}{p},$$

which can be approximated by

$$\Delta t \approx \frac{L}{2cp^2}(m_K^2-m_\pi^2) = \frac{2071}{p^2}\ \text{ps}.$$

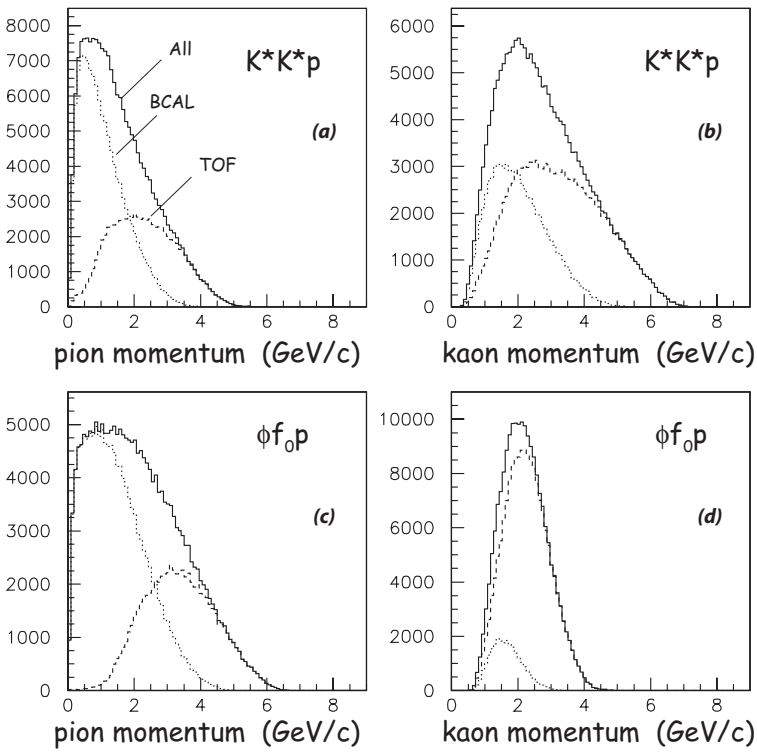

Figure 32: Momentum spectra shown separately for $\pi^{\pm}$ and $K^{\pm}$ for the final states $K^*(890)\bar{K}^*(890)p$ and $\phi f_0(980)p$. The light dashed histograms are for particle hitting the BCAL and the darker dashed for the forward time-of-flight, while the solid histograms are the sum (figure taken from reference [45]).

This can be used to examine the separation of kaons and pions in the TOF [49]. Figure 33 shows this separation for the first and fourth reaction above. The black curves labeled by timing resolution correspond to the number of σ of separation at the given momentum (read out on the left-hand vertical axis). The colored curves correspond to the integral of the momentum distribution (right-hand vertical scale). A 100 ps timing resolution would correspond to a 4σ separation for pions and kaons for momentum up to 2.5 GeV/c. As the particle momentum begins to rise above about 2 GeV/c, the ability of the TOF wall to separate pions and kaons decreases.

To study the timing in the BCAL [1], we generated events to simulate the reaction $\gamma p \rightarrow \pi^+\pi^-\pi^0 n$, where the 3π result from the decay $a_2(1320) \rightarrow \rho\pi$ or $\pi_2(1670) \rightarrow f_2\pi$ with a $e^{-5\cdot|t|}$. The charged particles were tracked through a uniform magnetic field and for $\pi^{\pm}$ reaching the BCAL, the π/K difference was computed (see Figure 34). Clearly, a 200 ps mean-time resolution does not allow for efficient π/K separation in the BCAL. For protons reaching the BCAL, the π/p time difference is also shown. Here, the 200 ps resolution provides very good separation of pions and protons.

The protons from the reactions of interest in GlueX tend to be observed in the central region of the detector (see Figure 25). While most of these will yield a timing signal in the BCAL, those with transverse momentum smaller than 300 MeV/c will spiral such that they will not hit the BCAL. For those that have low total momentum, a dE/dx measurement in the CDC may be the

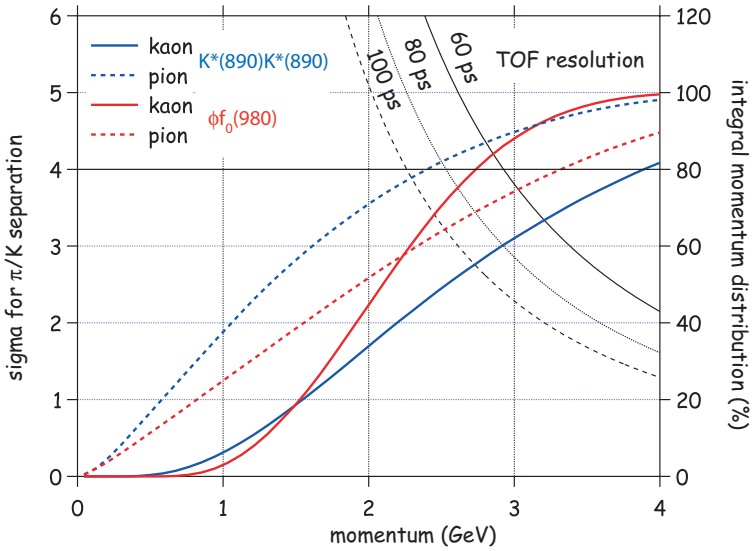

Figure 33: The expected π/K separation using the forward TOF as a function of momentum compared to the integral momentum spectrum. The blue curves correspond to the reaction $\gamma p \to pK^*(890)K^*(890)$, while the red curves correspond to the $\gamma p \to pf_0(980)\phi(1020)$. Both reactions populate the final state $p\pi^+\pi^-K^+K^-$ (figure take from reference [49]).

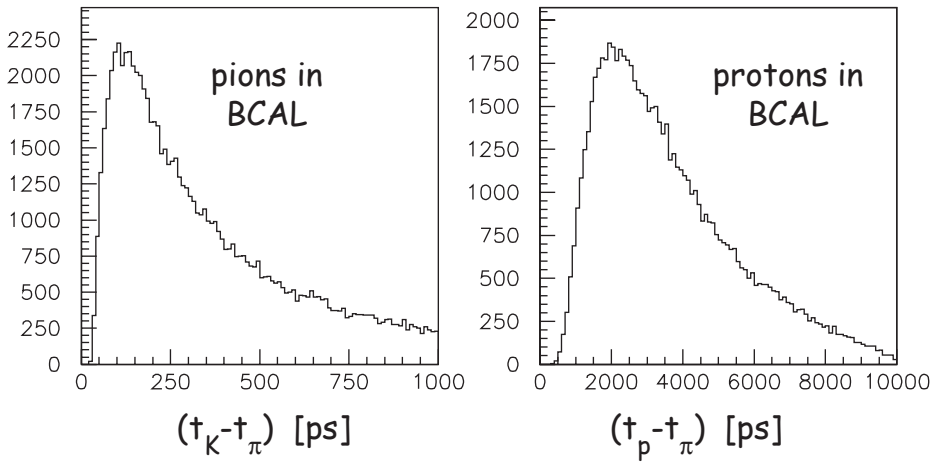

Figure 34: (a) The distribution in pion/kaon time difference for $\pi^\pm$ reaching the BCAL from the reaction $\gamma p \to \pi^+\pi^+\pi^-p$; (b) the distribution in proton/pion time for the same reaction. The expected time resolution in the BCAL is 200 ps.

only PID measurement that we have. A study of this was performed using the reaction [50]

$$\gamma p \quad \to \quad pK^+K^-\pi^+\pi^- \, .$$

For this reaction, 90% of the protons were detected in the CDC and 66% of the protons were observed in both the BCAL and the CDC. Placing a 3σ cut on the BCAL timing, over 99% of the protons are correctly identified and only 0.2% of the pions leak into the proton sample. For the

CDC alone, the dE/dx is not expected to be quite this good. Here, it is found that 95% of the protons were correctly identified, but 15% of the pions were misidentified as protons. Combining these, GlueX is expected to have 90% efficiency for identifying protons and a 96% efficiency for rejecting pions. Performing the same study for the kaons, it is found that the signal to background is only about 16%. If GlueX would only use the individual detectors, an additional factor of about 20 would be needed in K/π separation, mostly in the forward region.

At turn on, the GlueX detector will be able to separate pions and protons and have some limited capability to identify kaons. The addition of supplementary particle identification such as a RICH detector in front of the TOF wall would allow this to be substantially improved.

6.2 Global event analysis

Individual particle identification systems provide a most probable assignment to a particle type based on information in a single detector. Because GlueX will study exclusive final states, physics principles such as strangeness conservation in conjunction with analysis tools such as kinematic fitting, can be used to make global particle assignments to all particles in an event. Studies with realistic resolutions in GlueX, in conjunction with kinematic fitting, are currently being carried out [51]. While these have not been fully completed the initial results indicate that improvements by factors of at least a few are possible. Experience from other detectors (such as CLAS) indicate that it is fairly easy to improve by a factor of several over simple particle-based particle identification.

As an example of how kinematic fitting can be applied, one could consider the following two reactions. In addition, one would want to add an appropriate admixture of PYTHIA background events.

$$\begin{aligned} \gamma p &\rightarrow p K^+ K^- \pi^+ \pi^- \\ \gamma p &\rightarrow p \pi^+ \pi^- \pi^+ \pi^- \end{aligned}$$

The first is a signature reaction for $s\bar{s}$ hybrids, while the second is a fairly prolific final state in GlueX.

When no particle identification is assumed, there are 15 ways to make particle assignments in the final state. All possible assignments would be kinematically fit and cuts on the resulting confidence level would be made. A combination is accepted if it has a confidence level of at least 10% for the correct hypothesis. A hypothesis is rejected if it has a confidence level that is less than 1%. An event would be claimed to be resolved if at the end of the 15 fits, only one hypothesis remained, and it had a confidence level larger than 10%. This can be improved by including a probabilistic identification for each particle based on measurements in the PID system.

In this way, kinematic fitting of exclusive final states can be used to arrive at a global identification of all particles in the final state. If rather than an exclusive final state, one particle is missing, the efficiency of this procedure will drop, but as it uses all available information in conjunction with constraints, it will do better than any individual assignment method.

While it is quite likely that the ability of GlueX to identify kaons will improve beyond the numbers quoted above, it is still likely that a complete program of strangeness physics will require an additional particle identification detector.

7 Conclusions

Photoproduction using linearly polarized photons at ≈ 9 GeV is expected to provide a rich hunting ground for exotic mesons. Little data on photoproduction exists at these energies, and that which does exist, provides almost no information on final states with multi-neutrals. Even where data do exist, GlueX should have statistics that are 4 to 5 orders of magnitude larger. The GlueX detector has been designed to carry out a broad program in gluonic excitation—a program that will require the complete detection of final states involving charged particles and photons. In addition to tracking charged particles, the analyses need complete calorimetry coverage and uniform acceptance in azimuthal angle around the beam line. The latter is to fully take advantage of the linearly polarized photons. This, coupled with the 9 GeV photon beam, imposes a cylindrical geometry for the detector. We have also shown that in terms of reconstructing quantities relevant to amplitude analysis, GlueX will perform at least as well as the Brookhaven E852 experiment. The latter demonstrated the ability to carry out high-statistics amplitude analysis and extract signals at the level of a few percent of strong signals. For much of the physics to be performed in GlueX, separating protons from pions will be essential. Here, we have shown that this can be easily done in GlueX as designed. The somewhat more difficult task of separating kaons looks to be difficult with the current detector. However, the inclusion of an additional PID element, such as a RICH would, very likely resolve this issue. Overall, the performance of GlueX will be sufficient to successfully search for exotic mesons in an essentially unexplored reaction.

References

[1] A. Dzierba, *et. al.* Physics an Calorimeter Performance metrics. Technical report, GlueX Collaboration, 2008. GlueX-doc-985.

[2] C. A. Meyer *et al.* Physics and Detector Performance Metrics. Technical report, GlueX Collaboration, 2008. GlueX-doc-999.

[3] Gunnar S. Bali et al. Static potentials and glueball masses from QCD simulations with Wilson sea quarks. *Phys. Rev.*, D62:054503, 2000.

[4] Y. Nambu. Technical report, University of Chicago, 1970. Report No. 70-70.

[5] Nathan Isgur and Jack E. Paton. A Flux Tube Model for Hadrons in QCD. *Phys. Rev.*, D31:2910, 1985.

[6] Claude W. Bernard et al. Exotic mesons in quenched lattice QCD. *Phys. Rev.*, D56:7039–7051, 1997.

[7] Thomas D. Cohen. Quantum number exotic hybrid mesons and large N(c) QCD. *Phys. Lett.*, B427:348–352, 1998.

[8] Eberhard Klempt and Alexander Zaitsev. Glueballs, Hybrids, Multiquarks. Experimental facts versus QCD inspired concepts. *Phys. Rept.*, 454:1–202, 2007.

[9] Andrei Afanasev and Philip R. Page. Photo- and electroproduction of $J^{PC} = 1^{-+}$ exotics. *Phys. Rev.*, D57:6771–6777, 1998.

[10] C. McNeile and C. Michael. Decay width of light quark hybrid meson from the lattice. *Phys. Rev.*, D73:074506, 2006.

[11] W.-M. Yao et al. Review of particle physics. *J. Phys.*, G33:1, 2006.

[12] H. H. Bingham et al. Total and partial γp cross sections at 9.3 GeV. *Phys. Rev.*, D8:1277–1286, 1973.

[13] J. Ballam et al. Vector meson production by polarized photons at 2.8, 4.7 and 9.3 GeV. *Phys. Rev.*, D7:3150–3177, 1973.

[14] Y. Eisenberg et al. Photoproduction of ω mesons from 1.2 to 8.2 GeV. *Phys. Lett.*, B34:439–442, 1971.

[15] Y. Eisenberg et al. Study of high energy photoproduction with positron-annihilation radiation. I. Three-prong events. *Phys. Rev.*, D5:15–38, 1972.

[16] G. Alexander et al. Study of high energy photoproduction with positron-annihilation radiation. II. The reaction $\gamma p \to p\pi^+\pi^+\pi^-\pi^-$. *Phys. Rev.*, D8:1965–1978, 1973.

[17] G. Alexander et al. Study of high energy photoproduction with positron-annihilation radiation. III. The reactions $\gamma p \to p2\pi^+2\pi^-\pi^0$ and $\gamma p \to n3\pi^+2\pi^-$. *Phys. Rev.*, D9:644–648, 1974.

[18] T. Sjöstrand, S. Mrenna, and P. Skands. Pythia 6.4 Physics and Manual. Technical report, Lund University, 2006. hep-ph/0603175 and http://www.thep.lu.se/~torbjorn/Pythia.html.

[19] A. Dzierba. Comparing Pythia Simulations with Photoproduction Data at 9 GeV. Technical report, GlueX Document, 2007. GlueX-doc-856.

[20] A. Dzierba. Three Pion Production in GlueX. Technical report, GlueX Collaboration, 2008. GlueX-doc-1006.

[21] A. R. Dzierba, *et al.* A partial wave analysis of the $\pi^-\pi^-\pi^+$ and $\pi^-\pi^0\pi^0$ systems and the search for a $J^{PC} = 1^{-+}$ meson. *Phys. Rev.*, D73:072001, 2006.

[22] D. Lawrence. Track fitting in GlueX: Development Report III. Technical report, GlueX Document, 2007. GlueX-doc-761.

[23] A. Dzierba. K_S Mass Errors Due to Tracking Resolution. Technical report, GlueX Collaboration, 2008. GlueX-doc-1007.

[24] C. A. Meyer and M. Williams. Kinematic Fitting in CLAS. Technical report, GlueX Collaboration, 2007. GlueX-doc-818.

[25] A. R. Dzierba, M. Shepherd and B. Zihlmann. FCAL: Forward Calorimeter. Technical report, GlueX Collaboration, 2008. GlueX-doc-988.

[26] B. B. Brabson et al. A study of two prototype lead glass electromagnetic calorimeters. *Nucl. Instrum. Meth.*, A332:419–443, 1993.

[27] R. R. Crittenden et al. A 3000 element lead-glass electromagnetic calorimeter. *Nucl. Instrum. Meth.*, A387:377–394, 1997.

[28] R. T. Jones et al. A bootstrap method for gain calibration and resolution determination of a lead-glass calorimeter. *Nucl. Instrum. Meth.*, A566:366–374, 2006.

[29] R. T. Jones et al. Performance of the RADPHI detector and trigger in a high rate tagged photon beam. *Nucl. Instrum. Meth.*, A570:384–398, 2007.

[30] F. J. Barbosa, E. Jastrzembski, H. Dong, J. Wilson, C. Cuevas and D. J. Abbott. A VME64X, 16-Channel, Pipelined, 250 MSPS Flash ADC with Switched, Serial (VXS) Extensions. *Proceedings 2007 IEE Nuclear Science Symposium*, page 831, 2007.

[31] A. R. Dzierba, G. J. Lolos and Z. Papandreou. BCAL: Barrel Calorimeter. Technical report, GlueX Collaboration, 2008. GlueX-doc-986.

[32] M. Adinolfi et al. The KLOE electromagnetic calorimeter. *Nucl. Instrum. Meth.*, A482:364–386, 2002.

[33] M. Adinolfi et al. The KLOE electromagnetic calorimeter. *Nucl. Instrum. Meth.*, A494:326–331, 2002.

[34] G. J. Lolos, Z. Papandreou and K. Zorn. SiPM for BCAL. Technical report, GlueX Collaboration, 2008. GlueX-doc-987.

[35] N. Kolev et al. Dependence of the spatial and energy resolution of BCAL on segmentation. Technical report, GlueX Document, 2007. GlueX-doc-659.

[36] B. Leverington. Analysis of the BCAL beam tests. Technical report, GlueX Document, 2007. GlueX-doc-804.

[37] R. Lindenbush. A study of the reaction $\pi^- p \to \eta\pi^0 n$ at 18 GeV/c. Ph. D. Thesis - Indiana University, 1998.

[38] A. R. Dzierba, *et ala*. A study of the $\eta\pi^0$ spectrum and search for a $J^{PC} = 1^{-+}$ exotic meson. *Phys. Rev.*, D67:094015, 2003.

[39] J. Ballam et al. Energy dependence of the reaction $\gamma p \to \rho^- \Delta^{++}$. *Phys. Rev.*, 26:995–997, 1971.

[40] C. A. Meyer and Y. van Harrlem. The GlueX Central Drift Chamber. Technical report, GlueX Collaboration, 2008. GlueX-doc-990.

[41] D. S. Carman and S. Taylor. Forward Drift Chamber Technical Design Report. Technical report, GlueX Collaboration, 2007. GlueX-doc-754.

[42] R. T. Jones. Detector Models for GlueX Monte Carlo Simulation: the CD2 Baseline. Technical report, GlueX Collaboration, 2006. GlueX-doc-732.

[43] D. Lawrence and S. Taylor. GlueX Simulation Geometry Version 4.0. Technical report, GlueX Collaboration, 2007. GlueX-doc-853.

[44] D. Lawrence. Track Fitting in GlueX : Development Report IV. Technical report, GlueX Collaboration, 2008. GlueX-doc-1004.

[45] A. Dzierba. A Summary of Kinematics Relevant to the GlueX Experiment. Technical report, GlueX Collaboration, 2007. GlueX-doc-853.

[46] E. S. Swanson P. R. Page and A. P. Szczepaniak. Hybrid Meson Decay Phenomenology. *Phys. Rev.*, D59:034016, 1999.

[47] K. Schilling, P. Seyboth, and G. Wolf. On the Analysis of Vector Meson Production by Polarized Photons. *Nuc. Phys.*, B15:397, 1970.

[48] B. Zihlmann. TOF detector description for CDR. Technical report, GlueX Collaboration, 2008. GlueX-doc-994.

[49] A. Dzierba. PID Introduction and TOF - Talk at March 2007 GlueX Meeting. Technical report, GlueX Collaboration, 2007. GlueX-doc-773.

[50] Eugene Chudakov. private communication, 2008.

[51] M. Bellis. A study of π-K separation using the kinematic fitter. Technical report, GlueX Collaboration, 2008. GlueX-doc-971.